Momentum distribution of charged particles in jets in dijet events in $p\bar{p}$ collisions at $\sqrt{s}=1.8$ TeV and comparisons to perturbative QCD predictions

D. Acosta,[13] T. Affolder,[24] H. Akimoto,[47] M. G. Albrow,[12] D. Ambrose,[34] D. Amidei,[26] K. Anikeev,[25] J. Antos,[1] G. Apollinari,[12] T. Arisawa,[47] A. Artikov,[10] T. Asakawa,[45] W. Ashmanskas,[9] F. Azfar,[32] P. Azzi-Bacchetta,[33] N. Bacchetta,[33] H. Bachacou,[24] W. Badgett,[12] S. Bailey,[17] P. de Barbaro,[38] A. Barbaro-Galtieri,[24] V. E. Barnes,[37] B. A. Barnett,[20] S. Baroiant,[5] M. Barone,[14] G. Bauer,[25] F. Bedeschi,[35] S. Behari,[20] S. Belforte,[44] W. H. Bell,[16] G. Bellettini,[35] J. Bellinger,[48] D. Benjamin,[11] J. Bensinger,[4] A. Beretvas,[12] J. Berryhill,[9] A. Bhatti,[39] M. Binkley,[12] D. Bisello,[33] M. Bishai,[12] R. E. Blair,[2] C. Blocker,[4] K. Bloom,[26] B. Blumenfeld,[20] S. R. Blusk,[38] A. Bocci,[39] A. Bodek,[38] G. Bolla,[37] Y. Bonushkin,[6] D. Bortoletto,[37] J. Boudreau,[36] A. Brandl,[28] C. Bromberg,[27] M. Brozovic,[11] E. Brubaker,[24] N. Bruner,[28] J. Budagov,[10] H. S. Budd,[38] K. Burkett,[17] G. Busetto,[33] K. L. Byrum,[2] S. Cabrera,[11] P. Calafiura,[24] M. Campbell,[26] W. Carithers,[24] J. Carlson,[26] D. Carlsmith,[48] W. Caskey,[5] A. Castro,[3] D. Cauz,[44] A. Cerri,[35] A. W. Chan,[1] P. S. Chang,[1] P. T. Chang,[1] J. Chapman,[26] C. Chen,[34] Y. C. Chen,[1] M.-T. Cheng,[1] M. Chertok,[5] G. Chiarelli,[35] I. Chirikov-Zorin,[10] G. Chlachidze,[10] F. Chlebana,[12] L. Christofek,[19] M. L. Chu,[1] J. Y. Chung,[30] W.-H. Chung,[48] Y. S. Chung,[38] C. I. Ciobanu,[30] A. G. Clark,[15] M. Coca,[38] A. P. Colijn,[12] A. Connolly,[24] M. Convery,[39] J. Conway,[40] M. Cordelli,[14] J. Cranshaw,[42] R. Culbertson,[12] D. Dagenhart,[46] S. D'Auria,[16] F. DeJongh,[12] S. Dell'Agnello,[14] M. Dell'Orso,[35] S. Demers,[38] L. Demortier,[39] M. Deninno,[3] P. F. Derwent,[12] T. Devlin,[40] J. R. Dittmann,[12] A. Dominguez,[24] S. Donati,[35] M. D'Onofrio,[35] T. Dorigo,[17] I. Dunietz,[12] N. Eddy,[19] K. Einsweiler,[24] E. Engels, Jr.,[36] R. Erbacher,[12] D. Errede,[19] S. Errede,[19] Q. Fan,[38] H.-C. Fang,[24] R. G. Feild,[49] J. P. Fernandez,[37] C. Ferretti,[35] R. D. Field,[13] I. Fiori,[3] B. Flaugher,[12] L. R. Flores-Castillo,[36] G. W. Foster,[12] M. Franklin,[17] J. Freeman,[12] J. Friedman,[25] Y. Fukui,[23] I. Furic,[25] S. Galeotti,[35] A. Gallas,[29] M. Gallinaro,[39] T. Gao,[34] M. Garcia-Sciveres,[24] A. F. Garfinkel,[37] P. Gatti,[33] C. Gay,[49] D. W. Gerdes,[26] E. Gerstein,[8] P. Giannetti,[35] K. Giolo,[37] M. Giordani,[5] P. Giromini,[14] V. Glagolev,[10] D. Glenzinski,[12] M. Gold,[28] J. Goldstein,[12] G. Gomez,[7] I. Gorelov,[28] A. T. Goshaw,[11] Y. Gotra,[36] K. Goulianos,[39] C. Green,[37] G. Grim,[5] C. Grosso-Pilcher,[9] M. Guenther,[37] G. Guillian,[26] J. Guimaraes da Costa,[17] R. M. Haas,[13] C. Haber,[24] S. R. Hahn,[12] C. Hall,[17] T. Handa,[18] R. Handler,[48] F. Happacher,[14] K. Hara,[45] A. D. Hardman,[37] R. M. Harris,[12] F. Hartmann,[21] K. Hatakeyama,[39] J. Hauser,[6] J. Heinrich,[34] A. Heiss,[21] M. Herndon,[20] C. Hill,[5] A. Hocker,[38] K. D. Hoffman,[9] R. Hollebeek,[34] L. Holloway,[19] B. T. Huffman,[32] R. Hughes,[30] J. Huston,[27] J. Huth,[17] H. Ikeda,[45] J. Incandela,[12,*] G. Introzzi,[35] A. Ivanov,[38] J. Iwai,[47] Y. Iwata,[18] E. James,[26] M. Jones,[34] U. Joshi,[12] H. Kambara,[15] T. Kamon,[41] T. Kaneko,[45] M. Karagoz Unel,[29] K. Karr,[46] S. Kartal,[12] H. Kasha,[49] Y. Kato,[31] T. A. Keaffaber,[37] K. Kelley,[25] M. Kelly,[26] R. D. Kennedy,[12] R. Kephart,[12] D. Khazins,[11] T. Kikuchi,[45] B. Kilminster,[38] B. J. Kim,[22] D. H. Kim,[22] H. S. Kim,[19] M. J. Kim,[8] S. B. Kim,[22] S. H. Kim,[45] Y. K. Kim,[24] M. Kirby,[11] M. Kirk,[4] L. Kirsch,[4] S. Klimenko,[13] P. Koehn,[30] K. Kondo,[47] J. Konigsberg,[13] A. Korn,[25] A. Korytov,[13] E. Kovacs,[2] J. Kroll,[34] M. Kruse,[11] V. Krutelyov,[41] S. E. Kuhlmann,[2] K. Kurino,[18] T. Kuwabara,[45] A. T. Laasanen,[37] N. Lai,[9] S. Lami,[39] S. Lammel,[12] J. Lancaster,[11] M. Lancaster,[24] R. Lander,[5] A. Lath,[40] G. Latino,[28] T. LeCompte,[2] Y. Le,[20] K. Lee,[42] S. W. Lee,[41] S. Leone,[35] J. D. Lewis,[12] M. Lindgren,[6] T. M. Liss,[19] J. B. Liu,[38] T. Liu,[12] Y. C. Liu,[1] D. O. Litvintsev,[12] O. Lobban,[42] N. S. Lockyer,[34] J. Loken,[32] M. Loreti,[33] D. Lucchesi,[33] P. Lukens,[12] S. Lusin,[48] L. Lyons,[32] J. Lys,[24] R. Madrak,[17] K. Maeshima,[12] P. Maksimovic,[20] L. Malferrari,[3] M. Mangano,[35] G. Manca,[32] M. Mariotti,[33] G. Martignon,[33] M. Martin,[20] A. Martin,[49] V. Martin,[29] J. A. J. Matthews,[28] P. Mazzanti,[3] K. S. McFarland,[38] P. McIntyre,[41] M. Menguzzato,[33] A. Menzione,[35] P. Merkel,[12] C. Mesropian,[39] A. Meyer,[12] T. Miao,[12] R. Miller,[27] J. S. Miller,[26] H. Minato,[45] S. Miscetti,[14] M. Mishina,[23] G. Mitselmakher,[13] Y. Miyazaki,[31] N. Moggi,[3] E. Moore,[28] R. Moore,[26] Y. Morita,[23] T. Moulik,[37] M. Mulhearn,[25] A. Mukherjee,[12] T. Muller,[21] A. Munar,[35] P. Murat,[12] S. Murgia,[27] J. Nachtman,[6] V. Nagaslaev,[42] S. Nahn,[49] H. Nakada,[45] I. Nakano,[18] R. Napora,[20] C. Nelson,[12] T. Nelson,[12] C. Neu,[30] D. Neuberger,[21] C. Newman-Holmes,[12] C.-Y. P. Ngan,[25] T. Nigmanov,[36] H. Niu,[4] L. Nodulman,[2] A. Nomerotski,[13] S. H. Oh,[11] Y. D. Oh,[22] T. Ohmoto,[18] T. Ohsugi,[18] R. Oishi,[45] T. Okusawa,[31] J. Olsen,[48] W. Orejudos,[24] C. Pagliarone,[35] F. Palmonari,[35] R. Paoletti,[35] V. Papadimitriou,[42] D. Partos,[4] J. Patrick,[12] G. Pauletta,[44] M. Paulini,[8] T. Pauly,[32] C. Paus,[25] D. Pellett,[5] L. Pescara,[33] T. J. Phillips,[11] G. Piacentino,[35] J. Piedra,[7] K. T. Pitts,[19] R. Plunkett,[12] A. Pompos,[37] L. Pondrom,[48] G. Pope,[36] T. Pratt,[32] F. Prokoshin,[10] J. Proudfoot,[2] F. Ptohos,[14] O. Pukhov,[10] G. Punzi,[35] J. Rademacker,[32] A. Rakitine,[25] F. Ratnikov,[40] D. Reher,[24] A. Reichold,[32] P. Renton,[32] A. Ribon,[33] W. Riegler,[17] F. Rimondi,[3] L. Ristori,[35] M. Riveline,[43] W. J. Robertson,[11] T. Rodrigo,[7] S. Rolli,[46] L. Rosenson,[25] R. Roser,[12] R. Rossin,[33] C. Rott,[37] A. Roy,[37] A. Ruiz,[7] A. Safonov,[5] R. St. Denis,[16] W. K. Sakumoto,[38] D. Saltzberg,[6] C. Sanchez,[30] A. Sansoni,[14] L. Santi,[44] H. Sato,[45] P. Savard,[43] A. Savoy-Navarro,[12] P. Schlabach,[12] E. E. Schmidt,[12] M. P. Schmidt,[49] M. Schmitt,[29] L. Scodellaro,[33] A. Scott,[6] A. Scribano,[35] A. Sedov,[37] S. Seidel,[28] Y. Seiya,[45] A. Semenov,[10] F. Semeria,[3] T. Shah,[25] M. D. Shapiro,[24] P. F. Shepard,[36] T. Shibayama,[45] M. Shimojima,[45] M. Shochet,[9] A. Sidoti,[33] J. Siegrist,[24] A. Sill,[42] P. Sinervo,[43] P. Singh,[19] A. J. Slaughter,[49] K. Sliwa,[46] F. D. Snider,[12] A. Solodsky,[39] J. Spalding,[12] T. Speer,[15] M. Spezziga,[42] P. Sphicas,[25] F. Spinella,[35] M. Spiropulu,[9] L. Spiegel,[12] J. Steele,[48] A. Stefanini,[35] J. Strologas,[19] F. Strumia,[15] D. Stuart,[12,*] K. Sumorok,[25] T. Suzuki,[45] T. Takano,[31] R. Takashima,[18] K. Takikawa,[45] P. Tamburello,[11] M. Tanaka,[45] B. Tannenbaum,[6] M. Tecchio,[26] R. J. Tesarek,[12] P. K. Teng,[1] K. Terashi,[39] S. Tether,[25] A. S. Thompson,[16] E. Thomson,[30] R. Thurman-Keup,[2] P. Tipton,[38] S. Tkaczyk,[12] D. Toback,[41] K. Tollefson,[27] A. Tollestrup,[12] D. Tonelli,[35] M. Tonnesmann,[27] H. Toyoda,[31] W. Trischuk,[43] J. F. de Troconiz,[17] J. Tseng,[25] D. Tsybychev,[13] N. Turini,[35] F. Ukegawa,[45]

T. Vaiciulis,[38] J. Valls,[40] E. Vataga,[35] S. Vejcik III,[12] G. Velev,[12] G. Veramendi,[24] R. Vidal,[12] I. Vila,[7] R. Vilar,[7] I. Volobouev,[24] M. von der Mey,[6] D. Vucinic,[25] R. G. Wagner,[2] R. L. Wagner,[12] W. Wagner,[21] N. B. Wallace,[40] Z. Wan,[40] C. Wang,[11] M. J. Wang,[1] S. M. Wang,[13] B. Ward,[16] S. Waschke,[16] T. Watanabe,[45] D. Waters,[32] T. Watts,[40] M. Weber,[24] H. Wenzel,[21] W. C. Wester III,[12] A. B. Wicklund,[2] E. Wicklund,[12] T. Wilkes,[5] H. H. Williams,[34] P. Wilson,[12] B. L. Winer,[30] D. Winn,[26] S. Wolbers,[12] D. Wolinski,[26] J. Wolinski,[27] S. Wolinski,[26] S. Worm,[40] X. Wu,[15] J. Wyss,[35] U. K. Yang,[9] W. Yao,[24] G. P. Yeh,[12] P. Yeh,[1] K. Yi,[20] J. Yoh,[12] C. Yosef,[27] T. Yoshida,[31] I. Yu,[22] S. Yu,[34] Z. Yu,[49] J. C. Yun,[12] A. Zanetti,[44] F. Zetti,[24] and S. Zucchelli[3]

(CDF Collaboration)

[1]*Institute of Physics, Academia Sinica, Taipei, Taiwan 11529, Republic of China*
[2]*Argonne National Laboratory, Argonne, Illinois 60439, USA*
[3]*Istituto Nazionale di Fisica Nucleare, University of Bologna, I-40127 Bologna, Italy*
[4]*Brandeis University, Waltham, Massachusetts 02254, USA*
[5]*University of California at Davis, Davis, California 95616, USA*
[6]*University of California at Los Angeles, Los Angeles, California 90024, USA*
[7]*Instituto de Fisica de Cantabria, CSIC–University of Cantabria, 39005 Santander, Spain*
[8]*Carnegie Mellon University, Pittsburgh, Pennsylvania 15218, USA*
[9]*Enrico Fermi Institute, University of Chicago, Chicago, Illinois 60637, USA*
[10]*Joint Institute for Nuclear Research, RU-141980 Dubna, Russia*
[11]*Duke University, Durham, North Carolina 27708, USA*
[12]*Fermi National Accelerator Laboratory, Batavia, Illinois 60510, USA*
[13]*University of Florida, Gainesville, Florida 32611, USA*
[14]*Laboratori Nazionali di Frascati, Istituto Nazionale di Fisica Nucleare, I-00044 Frascati, Italy*
[15]*University of Geneva, CH-1211 Geneva 4, Switzerland*
[16]*Glasgow University, Glasgow G12 8QQ, United Kingdom*
[17]*Harvard University, Cambridge, Massachusetts 02138, USA*
[18]*Hiroshima University, Higashi-Hiroshima 724, Japan*
[19]*University of Illinois, Urbana, Illinois 61801, USA*
[20]*The Johns Hopkins University, Baltimore, Maryland 21218, USA*
[21]*Institut für Experimentelle Kernphysik, Universität Karlsruhe, 76128 Karlsruhe, Germany*
[22]*Center for High Energy Physics, Kyungpook National University, Taegu 702-701, Korea,*
Seoul National University, Seoul 151-742, Korea,
and SungKyunKwan University, Suwon 440-746, Korea
[23]*High Energy Accelerator Research Organization (KEK), Tsukuba, Ibaraki 305, Japan*
[24]*Ernest Orlando Lawrence Berkeley National Laboratory, Berkeley, California 94720, USA*
[25]*Massachusetts Institute of Technology, Cambridge, Massachusetts 02139, USA*
[26]*University of Michigan, Ann Arbor, Michigan 48109, USA*
[27]*Michigan State University, East Lansing, Michigan 48824, USA*
[28]*University of New Mexico, Albuquerque, New Mexico 87131, USA*
[29]*Northwestern University, Evanston, Illinois 60208, USA*
[30]*The Ohio State University, Columbus, Ohio 43210, USA*
[31]*Osaka City University, Osaka 588, Japan*
[32]*University of Oxford, Oxford OX1 3RH, United Kingdom*
[33]*Universita di Padova, Istituto Nazionale di Fisica Nucleare, Sezione di Padova, I-35131 Padova, Italy*
[34]*University of Pennsylvania, Philadelphia, Pennsylvania 19104, USA*
[35]*Istituto Nazionale di Fisica Nucleare, University and Scuola Normale Superiore of Pisa, I-56100 Pisa, Italy*
[36]*University of Pittsburgh, Pittsburgh, Pennsylvania 15260, USA*
[37]*Purdue University, West Lafayette, Indiana 47907, USA*
[38]*University of Rochester, Rochester, New York 14627, USA*
[39]*Rockefeller University, New York, New York 10021, USA*
[40]*Rutgers University, Piscataway, New Jersey 08855, USA*
[41]*Texas A&M University, College Station, Texas 77843, USA*
[42]*Texas Tech University, Lubbock, Texas 79409, USA*
[43]*Institute of Particle Physics, University of Toronto, Toronto, Canada M5S 1A7*
[44]*Istituto Nazionale di Fisica Nucleare, University of Trieste/Udine, Italy*
[45]*University of Tsukuba, Tsukuba, Ibaraki 305, Japan*
[46]*Tufts University, Medford, Massachusetts 02155, USA*
[47]*Waseda University, Tokyo 169, Japan*
[48]*University of Wisconsin, Madison, Wisconsin 53706, USA*
[49]*Yale University, New Haven, Connecticut 06520, USA*

(Received 24 May 2002; published 23 July 2003)

Inclusive momentum distributions of charged particles in restricted cones around jet axes were measured in dijet events with invariant dijet masses in the range 80 to 600 GeV/c^2. Events were produced at the Fermilab Tevatron in $p\bar{p}$ collisions with a center of mass energy of 1.8 TeV and recorded by the Collider Detector at Fermilab. The results were compared to perturbative QCD calculations carried out in the framework of the modified leading log approximation (MLLA) and assuming local parton-hadron duality. It was shown that the data follow theoretical predictions quite well over the whole range of the jet energies included in this analysis. We extracted the MLLA cutoff scale Q_{eff} and found a value of 230 ± 40 MeV. The theoretical prediction of $E_{jet}\sin\theta_c$ scaling, where θ_c is the cone opening angle, was experimentally observed for the first time. From the MLLA fits to the data, two more parameters were extracted: the ratio of parton multiplicities in gluon and quark jets, $r=N^{g\text{-}jet}_{partons}/N^{q\text{-}jet}_{partons}=1.9\pm 0.5$, and the ratio of the number of charged hadrons to the number of predicted partons in a jet, $K^{charged}_{LPHD}=N^{charged}_{hadrons}/N_{partons}=0.56\pm 0.10$.

DOI: 10.1103/PhysRevD.68.012003 PACS number(s): 13.87.−a, 12.38.Qk

I. INTRODUCTION

We report a measurement of the inclusive momentum distributions of charged particles in dijet events with dijet invariant masses in the range 80 to 600 GeV/c^2. These events were produced at the Fermilab Tevatron in $p\bar{p}$ collisions with $\sqrt{s}=1.8$ TeV and recorded by the Collider Detector at Fermilab (CDF). The results are compared with perturbative QCD calculations carried out in the framework of the modified leading log approximation (MLLA) [1–6] and the hypothesis of local parton-hadron duality (LPHD) [7]. The MLLA evolution equations allow an analytical description of the development of a parton shower for gluon and quark jets. The LPHD hypothesis assumes that hadronization is local and occurs at the end of the parton shower development, so that properties of hadrons are closely related to those of partons. Altogether, the MLLA+LPHD scheme views jet fragmentation as a predominantly perturbative QCD process.

Modern Monte Carlo generators that use the leading log approximation (e.g. HERWIG [26]) were found to be very good in describing experimental data. However, one has to keep in mind that all generators are heavily tuned to reproduce the data. More generally, no matter how successful a Monte Carlo calculation is in describing data, it does not solve the physics problem of what is happening with QCD at low momentum transfers. Progress in this area is likely to come from perturbative QCD methods. If such methods are successful, they will greatly expand our understanding of the underlying physics of the jet fragmentation phenomenon.

The Tevatron data, with their broad range of jet energies, present a unique opportunity to verify the validity and consistency of the MLLA approach on an energy scale much larger than that available at other machines. Overlap of the energy regions of the Fermilab Tevatron and e^+e^- experiments allows a direct comparison of experimental results obtained in very different environments.

*Present address: University of California, Santa Barbara, California 93106.

II. THEORETICAL CONSIDERATIONS

A. Modified leading log approximation

The MLLA is a resummed perturbative calculation that keeps track of terms of order $\alpha_s^n\log^{2n}(E_{jet})$ and $\alpha_s^n\log^{2n-1}(E_{jet})$ at all orders n of perturbation theory (E_{jet} is the jet energy). Color coherence effects between diagrams of the same order in α_s can be accounted for by introducing an angular ordering [8] which effectively constrains sequentially emitted partons to successively smaller angles with respect to the parent parton. Angular ordering plays a very important role in building the resummation scheme at all orders and obtaining the final solutions in analytical form. Improved, more accurate solutions of the MLLA evolution equations are often referred to as ''next-to- . . . -MLLA,'' although technically they are of the same order. The MLLA and various next-to-MLLA versions differ in how they account for the orders beyond the precision stated above. They all do it only partially leading to the differences in their predictions (to be addressed at the end of this section).

Any theoretical model attempting to describe jet fragmentation phenomena must be able to handle particles with very low k_T scales. Here, k_T is defined as the transverse momentum of a particle with respect to the jet axis. Figure 1 shows the k_T distribution of charged particles in jets of mean energy $E_{jet}=108$ GeV and within a cone defined by the angle with respect to the jet axis $\theta_c=0.28$ rad. One can see that most of the particles have k_T's well below 1 GeV/c, i.e. in the domain where perturbative QCD calculations are not obviously applicable. In the MLLA, α_s, the coupling constant controlling emission of gluons, evolves as

$$\alpha_s=\frac{2\pi}{b}\frac{1}{\log(k_T/\Lambda_{QCD})}, \tag{1}$$

where b is a QCD constant that depends on the number of colors n_c and the number of flavors n_f of effectively massless quarks ($b=9$ for $n_c=3$ and $n_f=3$), and Λ_{QCD} is the QCD regularization scale. In order to carry out all intermediate stages of calculations, a sufficiently high cutoff scale Q_{cutoff} is imposed so that all partons are emitted with $k_T>Q_{cutoff}$, i.e. in a regime guaranteed to be perturbative. After the resummation is done, the final MLLA solutions for

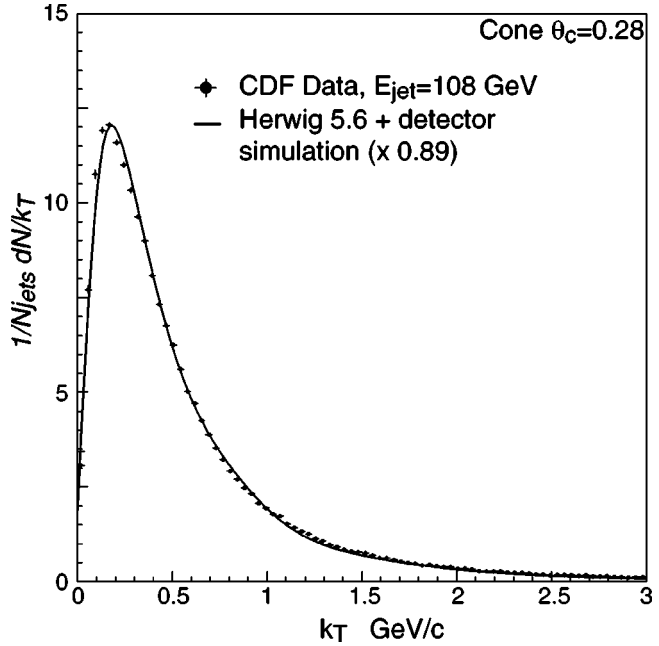

FIG. 1. Distribution of the momentum transverse to the jet axis for particles in cones of opening angle $\theta_c = 0.28$ rad around the jet axis, for mean energy $E_{jet} = 108$ GeV. Data points correspond to the CDF measurement described in this paper while the line was obtained from the HERWIG Monte Carlo plus detector simulation, scaled by a factor 0.89 as discussed in Sec. XIII.

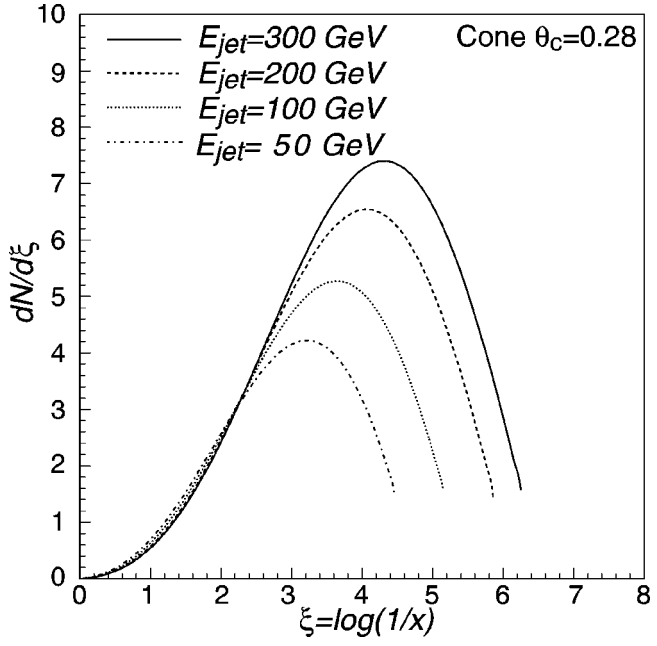

FIG. 2. The evolution of the MLLA predicted parton ξ spectrum with energy for a gluon jet and for a cone of opening angle $\theta_c = 0.28$ rad. The four lines correspond to jet energies $E_{jet} = 50$, 100, 200, and 300 GeV.

momentum distributions of partons are infrared stable with the cutoff parameter Q_{cutoff} as low as Λ_{QCD}. Lowering the parameter Q_{cutoff} is equivalent to including softer partons in the description of the model. Setting Q_{cutoff} to its lowest allowed value, Λ_{QCD}, maximizes the range of applicability of the model. The new phenomenological scale replacing the two initial parameters, Q_{cutoff} and Λ_{QCD}, is conventionally denoted as Q_{eff} and is the only parameter of the model.

The MLLA prediction for the shape of the momentum distribution of partons within an opening angle θ_c in a gluon jet of energy E_{jet} (Fig. 2) is given by [1,4]

$$\frac{dN_{partons}^{g\text{-}jet,MLLA}}{d\xi} = \frac{4n_c}{b}\Gamma(B)\int_{-\pi/2}^{\pi/2}\frac{d\tau}{\pi}e^{-B\alpha}\left\{\frac{\cosh\alpha+(1-2\zeta)\sinh\alpha}{\frac{4n_c}{b}Y\frac{\alpha}{\sinh\alpha}}\right\}^{B/2} I_B\left(\sqrt{\frac{4n_c}{b}Y\frac{\alpha}{\sinh\alpha}[\cosh\alpha+(1-2\zeta)\sinh\alpha]}\right), \tag{2}$$

where b is as defined earlier, B is another QCD constant ($B = 101/81$ for $n_c = 3$ and $n_f = 3$), and I_B is the modified Bessel function of order B. The other variables are

$$\xi = \log\frac{1}{x},\quad x = \frac{p}{E_{jet}},\quad Y = \log\frac{E_{jet}\sin\theta_c}{Q_{eff}},$$

$$\zeta = 1-\frac{\xi}{Y},\quad \alpha = \alpha_0 + i\tau,\quad \text{and}\quad \tanh\alpha_0 = 2\zeta - 1,$$

where p is the parton momentum.

This expression can be simplified to allow for easier manipulation [10]:

$$\frac{dN_{partons}^{g\text{-}jet,MLLA}}{d\xi} = \frac{8n_c}{\pi b}[2(1-\zeta)]^B\int_0^{\pi/2}d\tau(\cos\tau)^B \times\sum_{n=0}^{\infty}\frac{|a|^n}{n!}\frac{\Gamma(B)}{\Gamma(B+n+1)}\cos(n\phi - B\tau), \tag{3}$$

where

$$|a| = \frac{16n_c}{b}Y\zeta(1-\zeta)\cos\tau\sqrt{\frac{\alpha_0^2+\tau^2}{1-4\zeta(1-\zeta)\cos^2\tau}}$$

and

$$\phi = \tan^{-1}\left(\frac{(2\zeta-1)\tau - \alpha_0 \tan\tau}{(2\zeta-1)\alpha_0 + \tau\tan\tau}\right).$$

The shape of the MLLA inclusive parton momentum distributions can be approximated by a Gaussian [3] or a skewed Gaussian [11]. It should be pointed out that the MLLA equations are strictly valid for soft partons only ($x = p/E_{jet} \ll 1$). Although $dN/d\xi \to 0$ as $\xi \to 0$ as it should, the exact descent to zero is not expected to be well described by MLLA. MLLA also assumes that partons are massless and the opening angle θ_c is small.

The evolution of the momentum distribution peak position ξ_0 with jet energy is given by [6]

$$\xi_0 = \frac{1}{2}Y + \sqrt{cY} - c, \tag{4}$$

where $c = 0.29$ for $n_f = 3$.

Note that all the MLLA predictions depend on the combination $E_{jet}\sin\theta_c/Q_{eff}$, which implies the presence of scaling behavior.

Within MLLA, the momentum distribution of partons in a quark jet differs from that in a gluon jet only by a normalization factor $r = C_A/C_F = 9/4$ (C_A and C_F are the color charges of gluons and quarks, respectively):

$$\frac{dN^{q\text{-}jet}_{partons}(\xi)}{d\xi} = \frac{1}{r}\frac{dN^{g\text{-}jet}_{partons}(\xi)}{d\xi}. \tag{5}$$

More accurate solutions of the set of coupled QCD evolution equations describing parton production in quark and gluon jets primarily affect parton multiplicities. The corresponding changes are equivalent to rescaling the normalization of Eqs. (2), (3) by a factor F_{nMLLA}:

$$\frac{dN^{g\text{-}jet,nMLLA}_{partons}(\xi)}{d\xi} = F_{nMLLA}(E_{jet})\frac{dN^{g\text{-}jet,MLLA}_{partons}(\xi)}{d\xi}. \tag{6}$$

At the same time, the ratio of the number of partons in gluon and quark jets deviates from the lowest order value of 9/4. Like F_{nMLLA}, r becomes a function of the jet energy.

$F_{nMLLA}(E_{jet})$ and $r(E_{jet})$, when calculated analytically, are usually expressed in powers of $\sqrt{\alpha_s(E_{jet})}$. Improved "next-to- . . . -MLLA" calculations published in [12–14] disagree (see Figs. 3 and 4) on the exact scale of these corrections. However, they all suggest that both F_{nMLLA} and r are weak functions of energy. This allows the corrections to be treated as effectively constant for the range of dijet masses covered by this analysis. We assumed $F_{nMLLA} = 1.3$ with a ± 0.2 theoretical uncertainty (the range is shown as a shaded rectangle in Fig. 3). As for the parameter r, one may attempt to extract it from the data. This could serve two purposes. First, to verify the consistency of the MLLA calculations by checking if the values of r are in agreement with the expectations, and second, to try to distinguish between the three theoretical calculations [12–14] (see Fig. 4). With this in mind, we chose to treat r in this analysis as a free, energy-independent parameter.

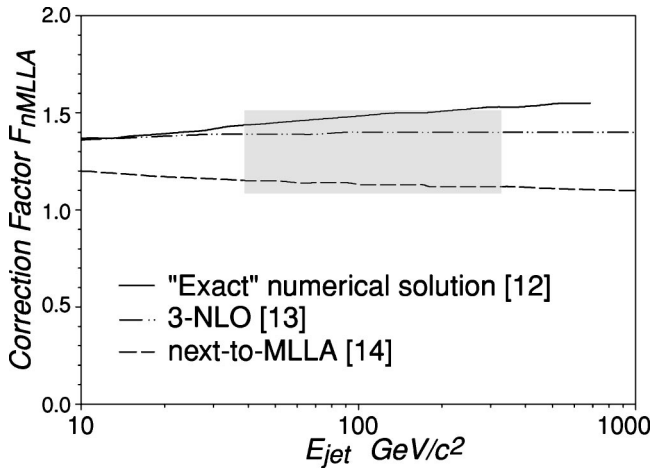

FIG. 3. Energy evolution of the correction factor F_{nMLLA} for the gluon jet, based on improved calculations with respect to MLLA [12–14] (shown as solid, dot-dot-dashed and dashed lines, respectively). The shaded area indicates the spread in calculated values of F_{nMLLA} for the range of energies relevant to this analysis.

B. Local parton-hadron duality

Any parton level calculation for jet fragmentation will be difficult to interpret if hadronization effects dominate the perturbative stage. An example of a hadronization model that preserves the correspondence between the properties of hadrons and partons is the LPHD hypothesis. LPHD has been shown to be naturally connected with the "pre-confinement" properties of QCD cascades [15]. Experimental studies are required to determine the lower limit at which the LPHD approach is applicable for hadronization.

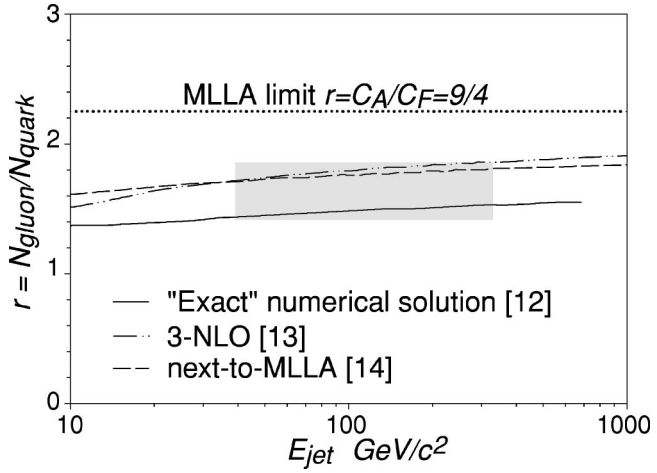

FIG. 4. Energy evolution of the ratio of parton multiplicities in gluon and quark jets based on improved calculations with respect to the MLLA [12–14] (shown as solid, dot-dot-dashed and dashed lines, respectively). The shaded area indicates the spread in calculated values of r for the range of energies relevant to this analysis.

Within LPHD, one relates the number of hadrons and their momentum distributions to those of partons via an energy-independent constant K_{LPHD}:

$$N_{hadrons} = K_{LPHD} \times N_{partons} \tag{7}$$

and

$$\frac{dN_{hadrons}}{d\xi} = K_{LPHD} \times \frac{dN_{partons}}{d\xi}. \tag{8}$$

In the simplest interpretation of LPHD, each parton produced during the perturbative stage picks up a color partner from the vacuum sea at the end of parton branching and binds into a hadron, so that $K_{LPHD} = N_{hadrons}/N_{partons} \simeq 1$. Then, for charged particles only, one expects from isospin invariance that the constant $K_{LPHD}^{charged} = N_{hadrons}^{charged}/N_{partons}$ should be approximately 2/3. Furthermore, assuming the fraction of the jet energy carried by particles in a jet to be charge independent, the fraction of charged particles with respect to all particles should be equal to the average fraction of the jet energy carried by charged particles. The latter has been measured in hadronic events at e^+e^- experiments to be approximately 0.60 [16], while the results from hadron colliders are $0.47 \pm 0.02 \pm 0.05$ [17] and $0.65 \pm 0.02 \pm 0.08$ [18].

C. Quark and gluon jets

Dijet events at the Fermilab Tevatron consist of both quark and gluon jets. By denoting the fractions of gluon and quark jets as ϵ_g and ϵ_q, respectively, one can rewrite the formula for the parton momentum distribution shape as follows:

$$\frac{dN_{partons}^{mix}}{d\xi} = \epsilon_g \frac{dN_{partons}^{g\text{-}jet}}{d\xi} + \epsilon_q \frac{dN_{partons}^{q\text{-}jet}}{d\xi} = \left(\epsilon_g + (1-\epsilon_g)\frac{1}{r} \right) \times \frac{dN_{partons}^{g\text{-}jet}}{d\xi}. \tag{9}$$

Combining this formula with Eq. (8) and taking into account the next-to-MLLA correction [Eq. (6)], one arrives at an expression for the shape of the momentum distribution expressed in terms of the MLLA spectrum [Eqs. (2), (3)]:

$$\frac{dN_{hadrons}^{charged}}{d\xi} = K \times \frac{dN_{partons}^{g\text{-}jet,MLLA}(\xi)}{d\xi} \tag{10}$$

with a normalization parameter K defined as

$$K = K_{LPHD}^{charged} \times F_{nMLLA} \times \left(\epsilon_g + (1-\epsilon_g)\frac{1}{r} \right). \tag{11}$$

III. EARLIER EXPERIMENTAL RESULTS

Comparisons of momentum distributions observed in data to the MLLA predictions have been performed in several e^+e^- and ep experiments and show good qualitative agreement. The distributions were fitted for the value of the Q_{eff} parameter and the normalization factor $K_{LPHD}^{charged}$. Q_{eff} was found to have a value around 250 MeV [19–21]. On the other hand, the measurements of $K_{LPHD}^{charged}$ were too high (around 1.3) [21] to be consistent with one-to-one parton-hadron correspondence. However, it should be pointed out that the measurement of $K_{LPHD}^{charged}$ is directly coupled to assumptions about F_{nMLLA} and r. In earlier papers F_{nMLLA} was taken to be 1, while r was assumed to be equal to 9/4. If one takes into account the next-to-MLLA value $F_{nMLLA} \simeq 1.3$ and $r \simeq 1.6$, the reported $K_{LPHD}^{charged}$ value needs to be rescaled, and its next-to-MLLA value becomes $\simeq 0.7$.

Several measurements of the ratio r of charged particle multiplicities in gluon and quark jets have been made. Early measurements showed little difference between charged particle multiplicities in gluon and quark jets (i.e., $r=1$) [22]. Later, the reported numbers [23] varied from $r \simeq 1.1$ to $r \simeq 1.5$ with typically small uncertainties. The variations are likely to be due to different definitions of jets and regions of particle phase space used in the analyses, which makes the observables different and the comparison to the theory ambiguous.

IV. ANALYSIS STRATEGY

Motivated by the predictions of the MLLA, we performed an analysis to determine how the momentum distributions of charged particles in jets evolve with jet energy and the opening angle within which the particles are observed. We used a data sample consisting of two-jet events. Note that in hadron collisions, to compare data to theoretical predictions described by Eqs. (2), (3) one has to use the jet energy measured in the center-of-mass system of the two jets. When referring to E_{jet} in this paper, we always assume it to be the jet energy in the center-of-mass frame of the two jet system. Assuming that jets are massless, $E_{jet} = M_{JJ}/2$, where M_{JJ} is the dijet mass (the exact definition can be found in Sec. VIII). Therefore, the events were assigned to nine bins according to their dijet masses. Momentum distributions were measured for particles in restricted cones of three sizes around the jet axis. The cones were selected to be sufficiently small so that $\theta_c \simeq \sin\theta_c$. The particular choices of $\theta_c = 0.28$, 0.36, and 0.47 rad were made to match the definition of the dijet mass bins. Consecutive cone sizes and the edges of the dijet mass bins were a factor of 1.3 apart from each other. This was motivated by the predicted $E_{jet}\theta_c/Q_{eff}$ scaling of the momentum distributions.

The measured distributions were fitted with the MLLA predicted spectrum, Eq. (10) with the parton spectrum as in Eq. (3), for the MLLA parameter Q_{eff} and normalization K. Values of Q_{eff} obtained from all combinations of dijet masses and cone sizes were compared to verify whether Q_{eff} is indeed universal. The evolution of K with energy, which comes mostly through the gluon fraction ϵ_g, Eq. (11), allowed extraction of the LPHD parton-to-hadron conversion parameter $K_{LPHD}^{charged}$ and the ratio of the multiplicities in gluon and quark jets, r.

Finally, the momentum distributions were fitted for the peak position ξ_0, and the evolution of ξ_0 with jet energy and cone size was plotted to verify the predicted $E_{jet}\sin\theta_c/Q_{eff}$ scaling. Measured peak positions were also used to extract

the parameter Q_{eff} using Eq. (II A). These extracted values of Q_{eff} were then compared to those obtained from the fit for the full shape of the distributions with the MLLA function, Eq. (10).

V. CDF DETECTOR

This analysis used data collected at the Collider Detector at Fermilab (CDF), a multipurpose detector designed for precision energy, momentum and position measurement of particles produced in proton-antiproton collisions with a center-of-mass energy of 1.8 TeV. The CDF detector is described in detail in [24] and references therein. Here, we will briefly describe the elements of the detector directly related to this analysis.

The CDF coordinate system is defined with respect to the proton beam direction, which defines the positive z direction, while the azimuthal angle ϕ is measured around the beam axis. The polar angle θ is measured with respect to the positive z direction. The pseudorapidity, η, is often used and is defined as $\eta = -\ln\tan(\theta/2)$. Transverse components of particle energy and momentum are conventionally defined as projections onto the plane transverse to the beam line, $E_T = E\sin\theta$ and $p_T = |\vec{p}|\sin\theta$.

The sub-detectors we used were the silicon vertex detector (SVX), the vertex drift chamber (VTX), the central tracking chamber (CTC) and the central parts of the calorimeter system, namely the central electromagnetic (CEM), central hadronic (CHA) and wall hadronic (WHA) calorimeters.

The SVX is the component of the CDF detector that is the closest to the beam line. It provides precise determination of the vertex position in the transverse plane via $r-\phi$ tracking. The VTX surrounds the SVX and helps determine the z position of the primary vertex. SVX and VTX information was used to determine the position of the primary vertex and to distinguish particles produced in the primary interaction from background tracks and tracks from secondary interactions in the same bunch crossing.

The SVX and the VTX are mounted inside the cylindrical 3.2 m long central tracking chamber. The CTC is an open-cell drift chamber of 2.65 m outer diameter designed for precision measurement of particle trajectories. The determination of particle momenta is based on trajectory curvature and knowledge of the solenoidal magnetic field ($B = 1.4$ T). The chamber contains 84 layers of sense wires grouped into nine superlayers. Five of the superlayers consist of 12 axial wires, while four stereo superlayers consist of six wires tilted by 3° with respect to the beam line. The CTC fully covers the region $-1<\eta<1$ with a momentum resolution better than $\delta p_T/p_T^2 \leqslant 0.002\ (\mathrm{GeV}/c)^{-1}$. In this analysis, we used particles in restricted cones around the jet axis, and particle momenta were measured entirely by the CTC.

The CEM is a lead-scintillator calorimeter, while the CHA and WHA consist of alternating iron and scintillator sheets. The CEM, CHA, and WHA have 2π azimuthal coverage, with pseudorapidity $|\eta|<1.1$ for the CEM and $|\eta|<1.3$ for the CHA+WHA. The segmentation of all three detectors is determined by the size of the individual towers, each covering 15° in ϕ and 0.1 unit in η. The CHA and CEM single particle energy resolutions are $0.5/\sqrt{E_T}\oplus 0.03$ and $0.135/\sqrt{E_T}\oplus 0.02$, respectively, where E_T is the transverse energy in GeV. The WHA energy resolution is $0.75/\sqrt{E_T}\oplus 0.04$. For our data sample, the jet energy resolution of the combined CDF calorimeter system varied from 10% to 7% for jet energies from 40 to 300 GeV.

VI. JET DEFINITION

In this analysis, jet identification, direction and energy are completely based on the calorimeter information. CDF defines jets using a cone algorithm. Starting with the highest E_T tower, the algorithm forms preclusters from an unbroken chain of contiguous seed towers (any tower with transverse energy E_T above 1 GeV) provided the towers are within a window of 7×7 towers centered at the originating tower. If a tower is outside this window, it is used to form a new precluster. The coordinates of the precluster are calculated as E_T-weighted sums of the ϕ and η of the seed towers assigned to this precluster. Next, all towers with E_T above 0.1 GeV within $R=\sqrt{(\Delta\phi)^2+(\Delta\eta)^2}=0.7$ of the precluster are merged into a cluster. The centroid of this cluster is computed, a new cone of radius $R=0.7$ is drawn around it, and towers inside the cone are assigned to the cluster. The procedure is then repeated until a stable set of clusters is found.

The energy of a jet is defined as the sum of the energies of the towers belonging to the corresponding cluster. Corrections are applied to compensate for the non-linearity and non-uniformity of the energy response of the calorimeter, the energy deposited inside the jet cone from sources other than the parent parton, and the parent parton energy that radiates out of the jet cone. Full details of this procedure can be found in [25].

VII. MONTE CARLO SIMULATIONS

To verify that the event selection and track quality cuts do not produce unexpected biases, we used the HERWIG 5.6 Monte Carlo event generator [26] and the standard CDF Monte Carlo program package QFL that simulates the response of the detector. HERWIG uses leading log approximation calculations for parton branching and explicitly includes color coherence effects. For hadronization, HERWIG employs the cluster model, which combines partons into colorless clusters and decays them into lighter clusters and/or final hadrons according to the available phase space.

We used HERWIG in its default configuration in conjunction with the parton distribution function sets CTEQ4M [27] and CTEQ4HJ [28].

QFL is a package that simulates the passage of particles through the CDF detector subsystems, including γ conversions, multiple scattering, decays of long-lived particles in the material of the detector, and showers in the calorimeters. The output of the simulation with QFL matches the data formats. Standard event generators, such as HERWIG, can be used as input to QFL.

TABLE I. Definition of bins for the dijet mass.

Left edge (GeV/c^2)	Right edge (GeV/c^2)	N_{events}	Mean measured M_{JJ} (GeV/c^2)	Unsmeared M_{JJ} (GeV/c^2)
72	94	4148	82	78
94	120	1968	105	101
120	154	3378	140	133
154	200	12058	182	171
200	260	31406	229	216
260	340	23206	293	274
340	440	7153	378	351
440	570	1943	488	452
570	740	416	629	573

VIII. EVENT SELECTION

The results presented in this paper are based on data collected during the 1993–1995 running period with a total accumulated luminosity $\simeq 95$ pb^{-1}. Events were accumulated using single jet triggers with E_T thresholds of 20, 50, 70 and 100 GeV, the first three triggers being pre-scaled by 1000, 40 and 8 respectively.

First, the raw jet energies measured by the calorimeters were corrected as described in Sec. VI. To select clean dijet events, we required the presence of two well-balanced (within the calorimeter resolution) high E_T jets: $|\vec{E}_{T_{jet1}} + \vec{E}_{T_{jet2}}|/(E_{T_{jet1}} + E_{T_{jet2}}) < 0.15$. One or two additional jets were allowed when they were very soft, $(E_{T_{jet3}} + E_{T_{jet4}})/(E_{T_{jet1}} + E_{T_{jet2}}) < 0.05$; otherwise, possible biases could be introduced (for example, in events with high energy jets, a single track escaping a jet at a sufficiently large angle could be identified as a separate jet). Only events with both leading jets in the central region of the detector ($|\eta_{jet1,2}| < 0.9$) were retained for the analysis to ensure efficient track reconstruction. The maximum number of primary vertices allowed was two because selecting only single vertex events would have unnecessarily reduced the statistics. Generally, in the events with two vertices, one can unambiguously choose the right one by comparing how much energy and how many tracks point from each vertex to the clusters in the calorimeter. Also, the second vertex is soft in an overwhelming fraction of cases, which makes the separation very clear. In this study, for events with two vertices, a spatial separation of at least 12 cm between them was required to ensure unambiguous assignment of tracks to the vertices.

After the selection cuts, the sample consisted of approximately 100 000 dijet events. The events were further subdivided into nine bins according to the dijet mass energy as measured by the calorimeters and defined as

$$M_{JJ} = \sqrt{(E_1 + E_2)^2/c^4 - (\vec{P}_1 + \vec{P}_2)^2/c^2}. \qquad (12)$$

The bins had a uniform log-scale width $\Delta \ln M_{JJ} = 0.3$, which was always wider than the calorimeter resolution for the dijet mass determination, $\delta M_{JJ}/M_{JJ} \simeq 7$–$10\,\%$. Table I shows how the dijet mass bins were defined along with the mean measured values of the dijet masses. It also shows the mean values of dijet masses after correcting for detector resolution effects (see Sec. X).

We varied the selection cuts to verify that our measurements do not show any noticeable dependence on the selection procedure. For example, the number of primary vertices allowed was restricted to one, and all the measurements were repeated. In the same way, the number of jets allowed was restricted to exactly two, and the jet E_T balancing requirements were varied. In addition, the fiducial cuts on jet η were varied by excluding the very central region ($|\eta| < 0.1$) and, separately, by excluding events with jets outside the region $|\eta_{1,2}| < 0.7$. The differences between the original values and those measured with varied selection cuts were used as estimates of the systematic uncertainties associated with the selection requirements.

To check that trigger effects do not bias the measurement, we verified the continuity of several observables in the dijet mass regions corresponding to the transition from one trigger to another. We analyzed the continuity of the inclusive mean multiplicity and the fraction of total jet energy carried by charged particles. These variables were chosen because the former one is sensitive to mismeasurements in the soft part of the particle spectra, while the latter is sensitive to high energy particles. No significant effects were found.

We also checked whether the analysis was sensitive to a particular choice of the cone radius R used by the jet finding algorithm. To do that, we selected events using different radii, 0.4 and 1.0 compared to the default value of 0.7, and keeping the rest of requirements unchanged. No significant variations in the results were observed.

IX. TRACK SELECTION, CORRECTIONS, AND SYSTEMATIC ERRORS

The analysis was carried out in the dijet center of mass frame. Momentum distributions were measured for tracks falling in restricted cones of sizes $\theta_c = 0.28$, 0.36, and 0.47 rad around the jet axis. Measured momentum distributions were normalized per jet. The following sections describe the track selection cuts and corrections that were applied to data. For illustration, we typically show the distribution corresponding to the middle dijet mass bin, with mean unsmeared $M_{JJ} = 216$ GeV/c^2. In cases where the energy dependence is

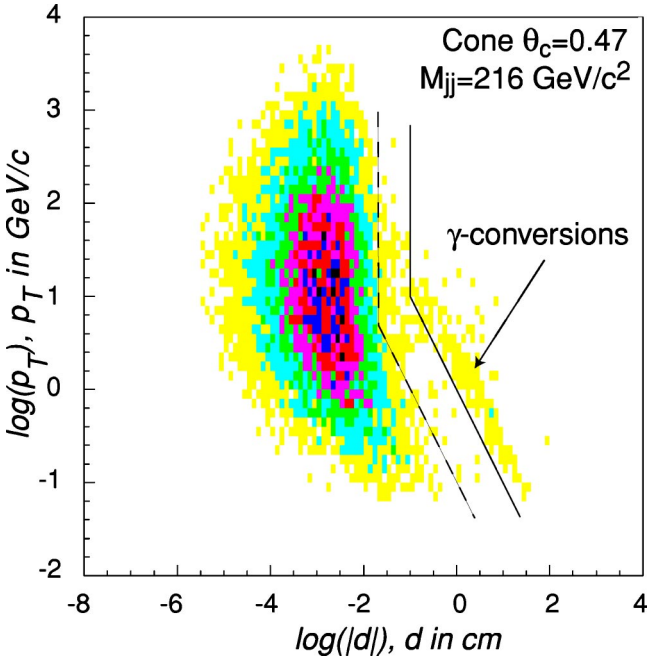

FIG. 5. The distribution of $\log p_T$ versus $\log|d|$ for the dijet mass bin with $M_{JJ}=216$ GeV/c^2. Here, p_T is the transverse momentum of the track and d is the impact parameter. The default cut on the impact parameter is shown by the solid line, while the cut shown by the dashed line was used to estimate the systematic error.

important, we show the data for the lowest and the highest dijet mass bins.

A. Track vertex cuts

We required full 3D track reconstruction and used several vertex cuts to ensure that tracks used in this analysis did originate from the primary vertex and were not due to secondary interactions, γ conversions, K^0 and Λ decays, or other backgrounds. The first vertex cut was on the track impact parameter, d, defined as the shortest distance in the r-ϕ plane between the interaction point as measured by the SVX/VTX detectors and the particle trajectory as obtained by the tracking algorithm fit. The second vertex cut used was on Δz, defined as the difference between the z position of the track at the point of its closest approach to the beam line and the position of the primary vertex, measured by the vertex detectors.

Figure 5 shows the distribution of $\log(p_T)$ versus $\log(|d|)$, where p_T is in GeV/c and d is in cm, for the data from the dijet mass bin with $M_{JJ}=216$ GeV/c^2. The cluster of points corresponds to particles produced at the interaction point or passing very close to it. The bend at the bottom of the main domain toward larger impact parameters corresponds to multiple scattering of low momentum particles.

The straight line of correlated points to the right of the main region corresponds to γ conversions. It can be shown that for electrons and positrons produced in γ conversions at radius R from the beam line, p_T and d have the following correlation:

$$\log P_T \simeq \log(0.15R^2B) - \log|d|, \tag{13}$$

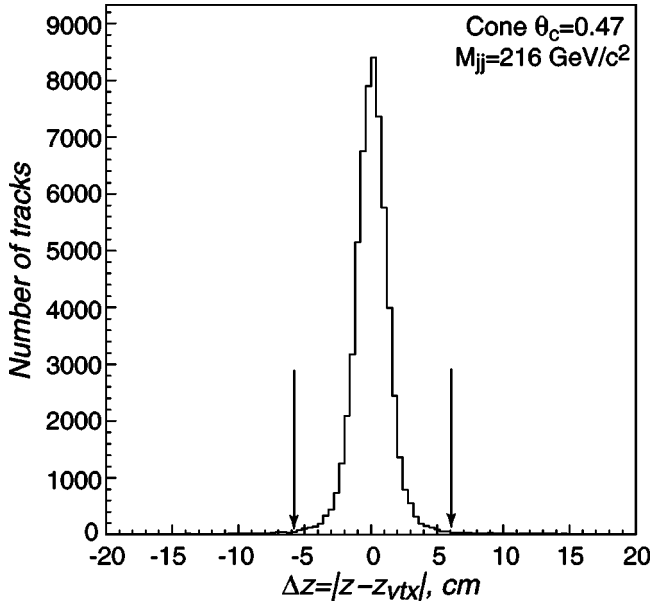

FIG. 6. The distribution of Δz (see the main text for definition) for tracks from the dijet mass bin with $M_{JJ}=216$ GeV/c^2 within a cone of opening angle $\theta_c=0.47$ rad.

where R is measured in meters and the magnetic field B is in tesla. In our case, the origin of the correlation was traced to cables in the area between the VTX and the CTC chambers. This was confirmed by detector simulation.

The nominal cut on the impact parameter removed the tracks produced by γ conversions (solid line on the plot) and all background tracks to the right of the γ-conversion line. Moving this cut further to the left would remove more of the background but would also eliminate signal tracks from the tails of the impact parameter resolution spectrum. To estimate the associated systematic error, we used another, harder cut eliminating everything outside the detector resolution errors (dashed line). For all measured values, the difference between using the default and the strict cut was conservatively assigned to be the systematic uncertainty associated with the impact-parameter requirements.

The parameter Δz was used to ensure that tracks from secondary interactions in the same bunch crossing were not assigned to the primary vertex. It was found that a cut $|\Delta z|<6$ cm was highly effective in eliminating tracks not originating from the primary vertex. Figure 6 shows the distribution of Δz for tracks falling in the cone with $\theta_c=0.47$ rad from the dijet mass bin with $M_{JJ}=216$ GeV/c^2. The $|\Delta z|<6$ cm criterion motivated the requirement $|z_1-z_2|>12$ cm on the spatial separation of primary vertices in two-vertex events used in the event selection described earlier.

B. CTC efficiency correction

We also had to correct for the CTC track reconstruction efficiency. Particles in jets of high energies tend to be spatially densely packed, which complicates pattern recognition. Sometimes, two tracks can be identified as one or lost altogether. This may also alter the reconstructed track parameters.

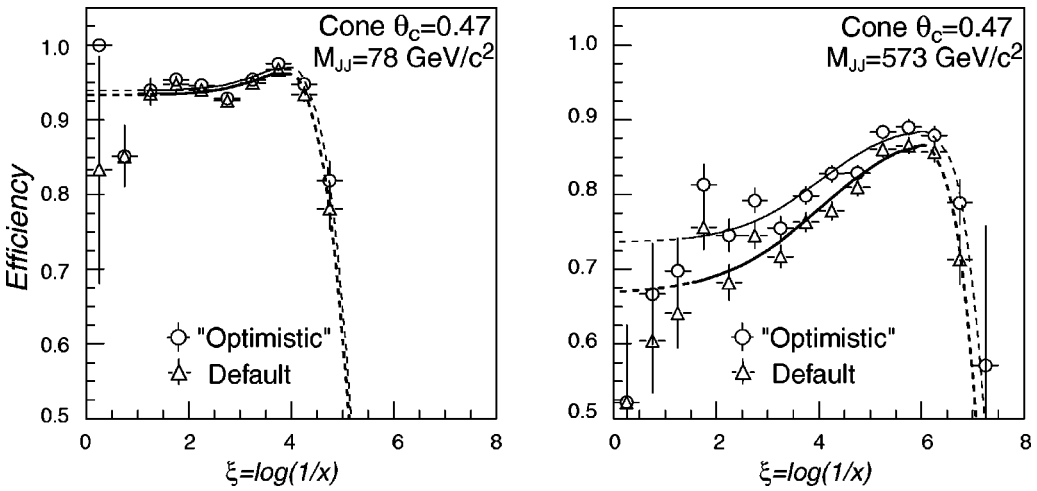

FIG. 7. The estimated CTC efficiency for tracks falling into the cone of opening angle $\theta_c = 0.47$ rad for the lowest and the highest dijet mass bins ($M_{JJ} = 78$ and 573 GeV/c^2). The upper line shows the ''optimistic'' scenario while the lower line corresponds to the default case. The $\xi = 1.6$ left end point of the lines corresponds to the fitting range used. The right end point is different for different dijet mass bins and cone sizes.

To investigate tracking reconstruction efficiencies, we used a procedure based on embedding tracks at the CTC hit level into real events and re-running the full CTC track reconstruction. For this purpose, we selected a smaller, but statistically representative subset of data (approximately 500 events for each dijet mass bin). For a given event in the subset, a track was selected from one of the jets, rotated 180° in the center-of-mass system, and embedded into the other jet. The full CTC reconstruction was then re-applied. By comparing the parameters of the reconstructed tracks with their original values before the embedding, we could determine whether the embedded track had been properly reconstructed. This procedure was repeated for each track in each event of the subset, allowing us to derive an efficiency correction function.

We chose to embed tracks from real dijet events to ensure that no biases (due to specific properties of embedded tracks) would be introduced into the calculated correction functions. The algorithm used to estimate the efficiency required one to determine whether the embedded track is found irrespective of surrounding tracks. In some cases, such a determination could not be made reliably. For example, if the embedded track and a nearby track from the original event are very close, the tracking algorithm may mix the sense wire hits from both to reconstruct a single track. Sometimes, this newly reconstructed track may have parameters very different from those of the embedded and the original tracks, making it impossible to determine if the embedded track survived the reconstruction.

When looking for the embedded track after reconstruction, we allowed three options: ''lost,'' ''found'' and ''found with mismeasured parameters.'' Every track was assigned to one of the three categories using a χ^2 based on comparing the helix parameters of the embedded and reconstructed tracks. The momentum distribution of all found tracks (including those with mismeasured parameters) was then compared to the original momentum distribution before embedding in order to extract the correction functions.

As explained above, in a fraction of cases tracks could not be unambiguously assigned to any of the three categories. Assigning these questionable tracks to either ''lost'' or ''found with mismeasured parameters'' allowed ''default'' and ''optimistic'' parametrizations for the tracking inefficiency to be defined and provided an estimate of the systematic uncertainty.

The scale of the correction depended on the energy and the cone size because it is larger for higher energies and smaller cones. Figure 7 shows the obtained efficiency as a function of ξ for the lowest and highest dijet mass bins. The upper curve (f_+) corresponds to the ''optimistic'' scenario, while the lower line (f_0) corresponds to the default parametrization.

For charged tracks, the average default tracker efficiency with the vertex cuts of Sec. IX A and within the opening angle $\theta_c = 0.47$ rad around the jet axis was found to be 93% at the lowest dijet mass and 78% at the highest mass.

C. Uncorrelated background subtraction

Additional corrections to the data were needed for the underlying event, accelerator induced backgrounds, and secondary interactions in the same bunch crossing that occurred very close to the vertex of the primary event.

To estimate the number of these uncorrelated background tracks in the jet cone, we defined two complementary cones, as shown in Fig. 8. These cones were positioned at the same polar angle with respect to the beam line as the original jets and rotated in ϕ so that they were at 90° (i.e. as far as possible) with respect to the dijet axis. This can be done when the dijet axis is within $45° < \theta < 135°$. Cones formed in such a fashion are assumed to collect statistically the same uncorrelated background as the cones around the jets.

Figure 9 shows the momentum distribution of particles after background subtraction in the cone of size $\theta_c = 0.47$ rad for the dijet mass bin with $M_{JJ} = 216$ GeV/c^2 (upper histogram). Also shown is the momentum distribution

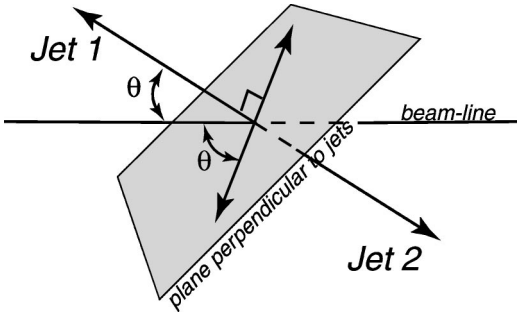

FIG. 8. Illustration of the definition of complementary cones. The unlabeled arrows are the axes of the cones complementary to jets 1 and 2.

of the background subtracted using the complementary cone defined above. The size of the correction was 0.5–0.6 tracks per jet for the cone of size $\theta_c = 0.47$ rad, and about 0.2 tracks for the cone with $\theta_c = 0.28$ rad.

Figure 10 shows the background spectra measured using the complementary cone technique as a function of $\log p$, where p is the track momentum in GeV/c, in the center-of-mass frame for the cone of size $\theta_c = 0.47$ rad, for three choices of dijet mass bins. Note that this correction is independent of the jet energy, in agreement with the assumption that this contribution is mostly due to uncorrelated backgrounds.

To evaluate uncertainties associated with background subtraction using the complementary cone technique, we used the following procedure. Background spectra were independently collected for all nine dijet mass bins. Then, for each given dijet mass bin, all nine background spectra (one by one) were subtracted from the raw momentum distribution for this dijet mass bin. The range of variation (maximum deviation from the original value) of the final results was assigned as the systematic error.

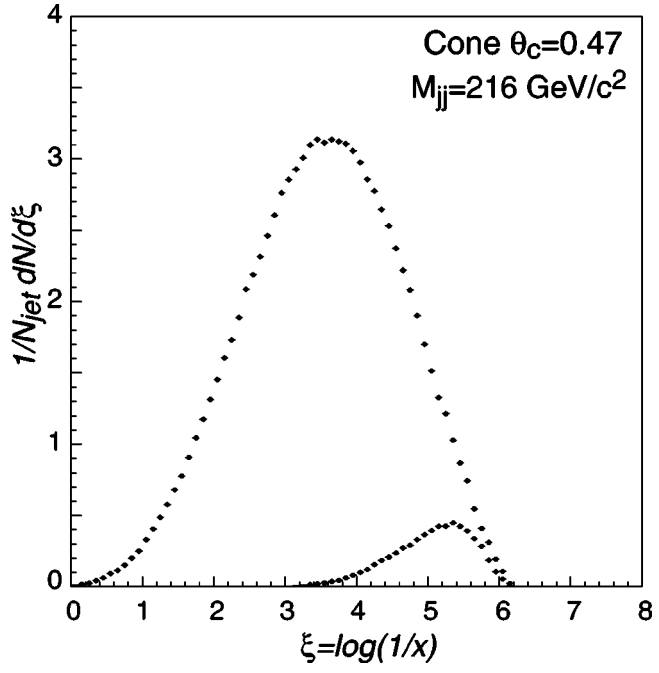

FIG. 9. Illustration of the complementary cone subtraction for the bin with dijet mass $M_{jj} = 216$ GeV/c^2 and cone with $\theta_c = 0.47$ rad. The upper histogram is the distribution after subtraction, while the lower one is the background contribution of the complementary cone that was subtracted.

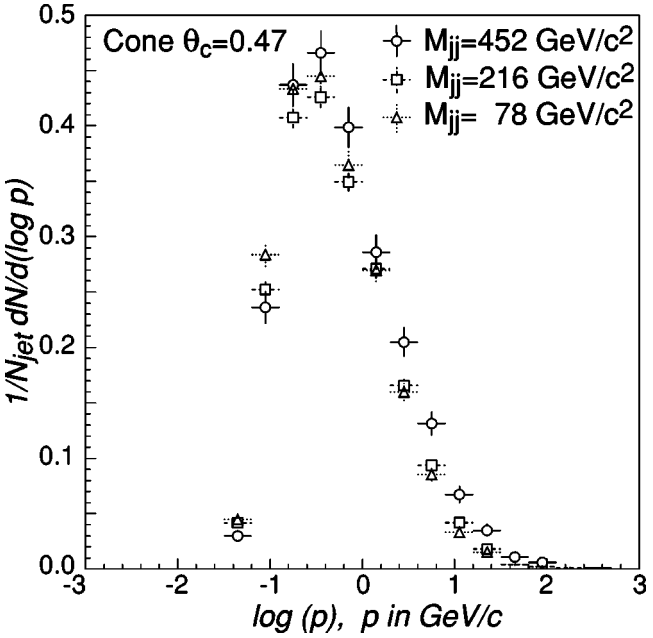

FIG. 10. Illustration of the complementary cone subtraction. The background spectra measured using the complementary cone technique as a function of $\log p$, where p is the track momentum in GeV/c. Three choices of dijet mass bins are shown ($M_{JJ} = 78$, 216 and 452 GeV/c^2) for tracks in the cone $\theta_c = 0.47$ rad around the complementary direction.

D. Correction for photon conversions

For the γ conversions that remained after the vertex cuts were applied, a correction to the momentum distribution was derived based on Monte Carlo studies. The correction was small ($\sim 3\%$) in the region where the distributions were fitted (see Fig. 11). This allowed us to conservatively estimate the associated uncertainty by comparing the results with and without this correction applied.

E. Jet reconstruction effects

To evaluate errors resulting from jet direction mismeasurement, we utilized Monte Carlo simulations. We compared the momentum distributions for two cases. In one case, the restricted cones were based on the jet direction as determined by the detector response from the simulation. Momentum distributions were produced using tracks in such cones. In the second case, we extracted the true jet direction as given by the HERWIG Monte Carlo program at the parton level. In this case, the momentum distributions were built using restricted cones around the true direction. Dividing one distribution by another, we obtained the desired bin-by-bin correction function.

Within the fitted range, the scale of the correction was consistent with unity, having a spread of approximately 1%

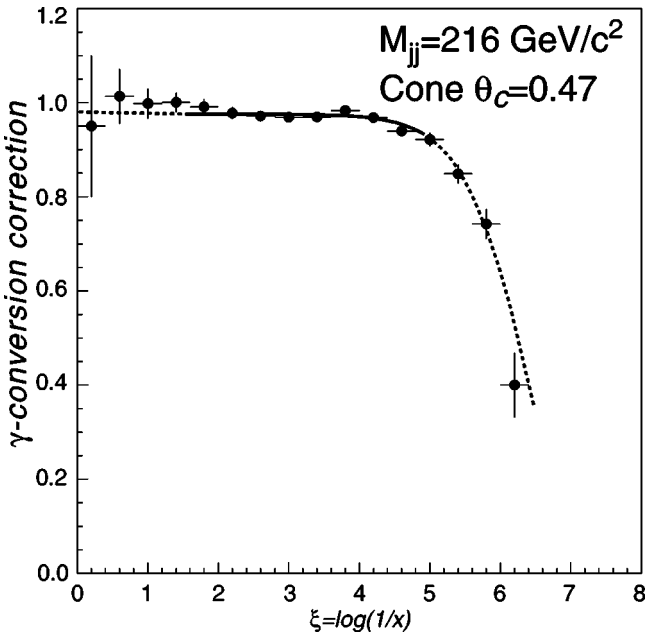

FIG. 11. Correction for the tracks from γ conversions that remained after the vertex cuts were applied. The dijet mass bin is $M_{JJ}=216$ GeV/c^2 and the cone size is $\theta_c=0.47$ rad. The solid line corresponds to the fitting range used.

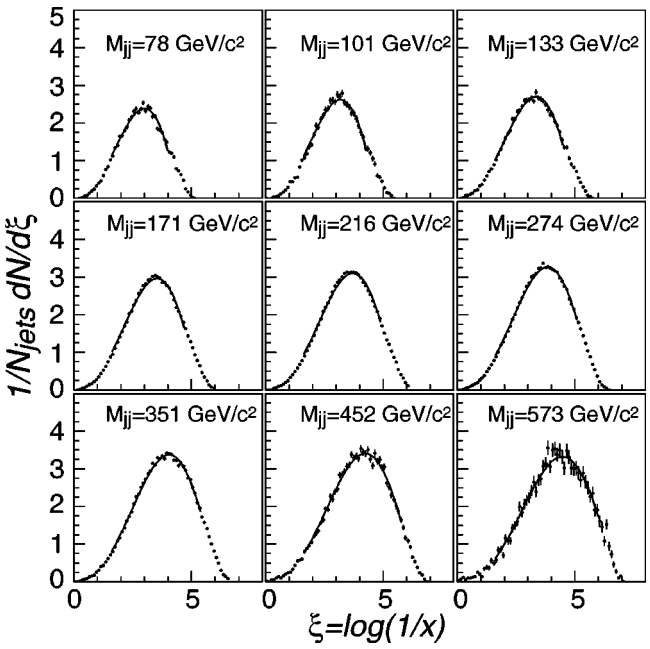

FIG. 12. Inclusive momentum distribution of particles in jets in the restricted cone of size $\theta_c=0.47$ rad for nine dijet masses. Each distribution is normalized per jet. The line represents the fit of the data to the MLLA gluon spectrum [Eq. (10)].

with no observed dependence on ξ. Because of the small scale of this correction, this effect was included in the estimates of the systematic uncertainty due to the jet direction mismeasurement but not explicitly corrected for.

The jet energy correction, mentioned in Sec. VI, accounts for several effects: the energy response of the calorimeter, the energy deposited inside the jet cone from sources other than the parent parton, and the parent-parton energy that radiates out of the jet cone. These corrections are standard for CDF and are described in detail elsewhere [25].

To estimate the systematic errors, we used parametrizations that under- or overestimate the jet energy and reclassified events according to dijet mass. The difference between the measurements for the default and modified distributions was assigned as systematic uncertainty.

X. MLLA FITS TO THE MOMENTUM DISTRIBUTIONS

The momentum distributions $dN/d\xi$, corrected for the various backgrounds and reconstruction inefficiencies described in the preceding section, were plotted in nine bins of dijet mass, as measured by the CDF calorimeter.

Since the energy resolution of the calorimeter is finite, in a specific dijet mass bin there is always a fraction of events that really originate in the nearby bins. This contamination causes a smearing of the $dN/d\xi$ distribution, which needs to be taken into account in comparisons with theoretical predictions [Eqs. (3) and (10)]. This was done as follows. For each experimental dijet mass bin we extracted the true dijet mass spectrum from the HERWIG simulation at the parton level, by selecting HERWIG events whose dijet mass, after detector simulation and reconstruction, falls within the given bin. The momentum distribution measured in a given bin was fitted with the theoretical prediction, Eqs. (3) and (10), averaged over the true dijet mass spectrum for that bin. The corresponding systematic uncertainty was estimated by comparing the above fit with a fit to Eq. (10) evaluated at the mean unsmeared dijet mass for the bin (i.e. no averaging).

Figures 12–14 show nine inclusive momentum distribu-

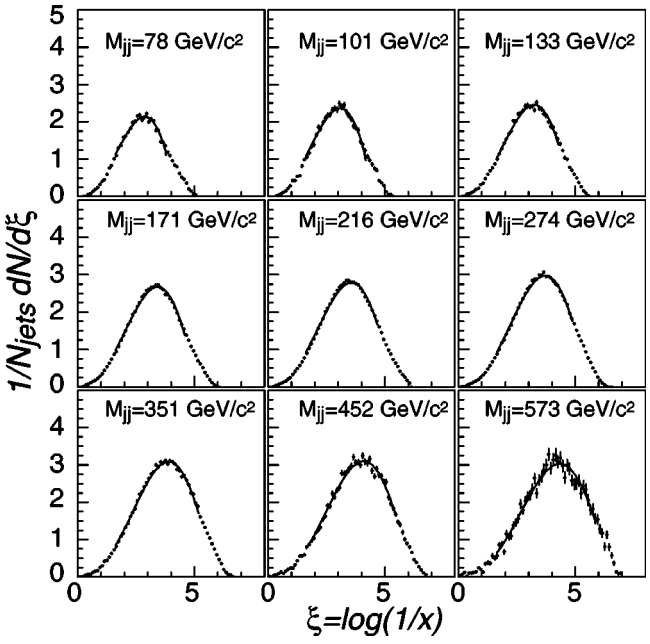

FIG. 13. Inclusive momentum distribution of particles in jets in the restricted cone of size $\theta_c=0.36$ rad for nine dijet masses. Each distribution is normalized per jet. The line represents the fit of the data to the MLLA gluon spectrum [Eq. (10)].

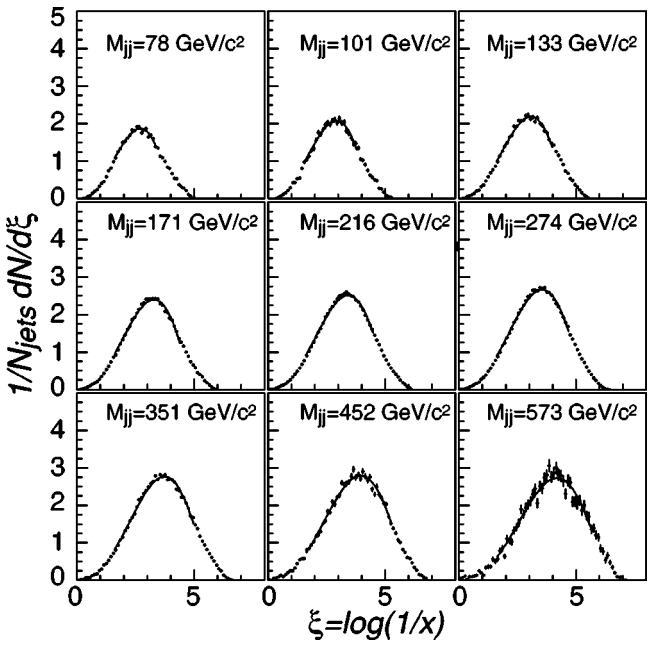

FIG. 14. Inclusive momentum distribution of particles in jets in the restricted cone of size $\theta_c=0.28$ rad for nine dijet masses. Each distribution is normalized per jet. The line represents the fit of the data to the MLLA gluon spectrum [Eq. (10)].

tions of charged particles corresponding to the nine available dijet mass bins and the restricted cone sizes $\theta_c=0.47$, 0.36, and 0.28 rad. The bin size in ξ was 0.1 and was chosen to be much wider than the resolution of the tracker within the fitted range. The lines correspond to the MLLA two-parameter fits according to Eq. (10). Table II contains the results of the fit, Q_{eff} and K.

When choosing the left edge of the fitting range, one needs to remember that the MLLA calculations are valid only for $x \ll 1$ (see Sec. 4). The default left edge of the fitting region was chosen to be $\xi=1.6$ ($x \simeq 0.2$).

On the other side of the spectrum, the MLLA imposes a limitation on the allowed transverse momentum k_T of the particles with respect to the jet ($k_T > Q_{eff}$). This results in a limit on the minimum allowed momentum of particles: $p = k_T/\sin\theta_c > Q_{eff}/\sin\theta_c$. The MLLA spectrum rapidly falls to zero at values of ξ exceeding $\xi_{max}=\log(E_{jet}\theta_c/Q_{eff})$. When fitting, the right edge was chosen to avoid this region.

The excluded regions contain tails of the momentum distributions with relatively small fractions of particles. By varying the left and right edges, we evaluated the systematic errors due to the choice of fitting range. These errors never dominated the overall systematic uncertainty.

Systematic uncertainties for the fitted parameters were estimated by varying the respective corrections and cuts and refitting the distributions for the parameters K and Q_{eff}. As an example, Table III shows the breakdown of the contributions of various systematic uncertainties for the fitted parameters for the cone of size $\theta_c=0.47$ rad and the dijet mass bin $M_{JJ}=216$ GeV/c^2.

The overall qualitative agreement between data and MLLA is very good. However, there is a small but statistically significant difference in shape between the data and the predictions, the data showing a steeper rise and fall around the peak (Figs. 12–14 and also Fig. 15) than the MLLA prediction. The values of the χ^2 shown in Table II are based on statistical errors only and refer to the distributions with all the default corrections and cuts described in Sec. IX.

We investigated whether these differences in shape could be accounted for by the systematic errors. For example, the CTC tracking correction, the largest correction applied to the data, was analyzed by refitting the momentum distributions using the CTC efficiency correction parametrized as follows:

$$f(p_{\mathrm{CTC}}) = f_0 + p_{\mathrm{CTC}}(f_+ - f_0),$$

where $p_{\mathrm{CTC}}=0$ corresponds to the default case ($f=f_0$), and the parametrization with $p_{\mathrm{CTC}}=+1$ ($f=f_+$) corresponds to the ''optimistic'' correction. We refitted the distributions treating p_{CTC} as a free parameter bounded by -1 and 1. The distributions were also re–fitted using the bin-by-bin CTC correction (shown as points on Fig. 7). No significant improvements in χ^2 were found.

XI. INTERPRETATION OF THE RESULTS

Figure 16 shows Q_{eff} obtained from the fits to the momentum distributions. One can see that Q_{eff} tends to become smaller for larger energies and, possibly, for smaller angles. The trends are statistically significant (the individual systematic uncertainties derived in different dijet mass bins are strongly correlated). The slight drift in the value of Q_{eff} may indicate the presence of higher order contributions and/or non-perturbative effects at the hadronization stage. However, the moderate scale of these variations suggests that the overall shape of the momentum distributions is, indeed, mostly governed by the perturbative stage of jet fragmentation.

For the final reported value of Q_{eff}, we calculated the mean of the 27 measurements shown in Fig. 16. The associated error is estimated by taking the difference between the maximum and minimum of the 27 values and dividing it by 2. After rounding off the result, we arrive at $Q_{eff}=230 \pm 40$ MeV. Note that this error covers the drift of the parameter Q_{eff}, which is not predicted by the theory. Therefore, the error should be interpreted as a range of values of Q_{eff} suitable for the dijet energies used in this analysis. Figure 16 also shows the results for the fitted parameter Q_{eff} from e^+e^- [19–21] and ep [29] data, showing good agreement and, possibly, the same trends.

Regarding the normalization parameter K, two considerations have to be addressed. First, according to Eq. (11), K depends linearly on ϵ_g, and fitting the distribution for the slope and intercept can resolve both $K_{LPHD}^{charged}$ and r. We also examine whether K remains cone size independent for a fixed dijet mass.

Although the value of Q_{eff} is completely defined by the shape of the distribution, Q_{eff} also affects the distribution amplitude: the smaller Q_{eff}, the higher the distribution. Therefore, the value of Q_{eff} is strongly correlated with the fitted value of K. If the shape of the distributions is not in perfect agreement with MLLA, the fit will try to tune Q_{eff} to improve the match. Since Q_{eff} is also tied to the amplitude

TABLE II. Fitted values of K and Q_{eff} (MeV) from inclusive momentum distributions of charged particles in cones of sizes 0.28, 0.36, and 0.47 rad around the jet axis for all available dijet mass samples. Each distribution was fitted independently. The first error is statistical and the second one is systematic. Note that the systematic uncertainties are strongly correlated.

Dijet mass (GeV/c^2)	Cone $\theta_c=0.28$	Cone $\theta_c=0.36$	Cone $\theta_c=0.47$
78	$K=0.590\pm0.005\pm0.059$	$K=0.611\pm0.004\pm0.043$	$K=0.634\pm0.004\pm0.048$
	$Q_{eff}=259\pm5\pm29$	$Q_{eff}=264\pm3\pm15$	$Q_{eff}=274\pm4\pm24$
	$\chi^2/d.f.=27/16$	$\chi^2/d.f.=56/20$	$\chi^2/d.f.=69/22$
101	$K=0.574\pm0.006\pm0.038$	$K=0.603\pm0.005\pm0.038$	$K=0.633\pm0.006\pm0.040$
	$Q_{eff}=239\pm5\pm20$	$Q_{eff}=242\pm4\pm12$	$Q_{eff}=263\pm4\pm14$
	$\chi^2/d.f.=26/20$	$\chi^2/d.f.=28/24$	$\chi^2/d.f.=39/25$
133	$K=0.560\pm0.004\pm0.037$	$K=0.577\pm0.004\pm0.037$	$K=0.596\pm0.004\pm0.038$
	$Q_{eff}=250\pm4\pm17$	$Q_{eff}=247\pm4\pm19$	$Q_{eff}=264\pm4\pm20$
	$\chi^2/d.f.=32/22$	$\chi^2/d.f.=47/25$	$\chi^2/d.f.=42/27$
171	$K=0.551\pm0.002\pm0.034$	$K=0.570\pm0.002\pm0.036$	$K=0.596\pm0.001\pm0.039$
	$Q_{eff}=229\pm2\pm12$	$Q_{eff}=235\pm2\pm12$	$Q_{eff}=253\pm2\pm18$
	$\chi^2/d.f.=106/26$	$\chi^2/d.f.=108/28$	$\chi^2/d.f.=132/29$
216	$K=0.536\pm0.001\pm0.037$	$K=0.551\pm0.001\pm0.039$	$K=0.569\pm0.001\pm0.042$
	$Q_{eff}=230\pm1\pm17$	$Q_{eff}=235\pm1\pm19$	$Q_{eff}=241\pm1\pm18$
	$\chi^2/d.f.=306/27$	$\chi^2/d.f.=357/29$	$\chi^2/d.f.=408/31$
274	$K=0.529\pm0.001\pm0.040$	$K=0.546\pm0.001\pm0.041$	$K=0.560\pm0.001\pm0.042$
	$Q_{eff}=233\pm1\pm21$	$Q_{eff}=237\pm1\pm15$	$Q_{eff}=247\pm1\pm18$
	$\chi^2/d.f.=169/29$	$\chi^2/d.f.=214/31$	$\chi^2/d.f.=230/33$
351	$K=0.503\pm0.001\pm0.048$	$K=0.516\pm0.002\pm0.043$	$K=0.521\pm0.002\pm0.044$
	$Q_{eff}=227\pm2\pm18$	$Q_{eff}=226\pm2\pm17$	$Q_{eff}=226\pm2\pm18$
	$\chi^2/d.f.=109/32$	$\chi^2/d.f.=85/34$	$\chi^2/d.f.=90/36$
452	$K=0.453\pm0.002\pm0.047$	$K=0.470\pm0.003\pm0.048$	$K=0.478\pm0.003\pm0.042$
	$Q_{eff}=204\pm3\pm19$	$Q_{eff}=211\pm4\pm22$	$Q_{eff}=212\pm3\pm17$
	$\chi^2/d.f.=76/35$	$\chi^2/d.f.=85/37$	$\chi^2/d.f.=79/39$
573	$K=0.394\pm0.006\pm0.049$	$K=0.406\pm0.006\pm0.049$	$K=0.415\pm0.003\pm0.050$
	$Q_{eff}=178\pm7\pm25$	$Q_{eff}=180\pm6\pm26$	$Q_{eff}=184\pm6\pm29$
	$\chi^2/d.f.=69/39$	$\chi^2/d.f.=61/41$	$\chi^2/d.f.=54/43$

TABLE III. Systematic uncertainties for dijet mass bin with $M_{JJ}=216$ GeV/c^2 and cone $\theta_c=0.47$ rad.

	MLLA fit		Peak position
Origin of uncertainty	σ_K/K	$\sigma_{Q_{eff}}/Q_{eff}$	σ_{ξ_0}/ξ_0
Statistical uncertainty	0.1%	0.4%	0.2%
Uncertainties related to the event selection:			
Cut on soft jets	0.2%	0.5%	0.0%
Cut on jet balance	0.4%	0.5%	0.1%
Cut on number of vertices	1.4%	0.9%	0.2%
Jet $\lvert\eta\rvert$ cut	0.4%	1.2%	0.1%
Other uncertainties:			
Track vertex cuts	5.5%	3.4%	0.5%
CTC efficiency	2.5%	1.7%	0.3%
Uncorrelated background	0.2%	0.1%	0.1%
γ-conversion correction	2.2%	2.7%	0.6%
Jet energy measurement (total)	3.5%	4.3%	0.7%
Jet direction measurement	0.3%	0.4%	0.1%
Choice of fitting range	1.1%	2.0%	0.2%

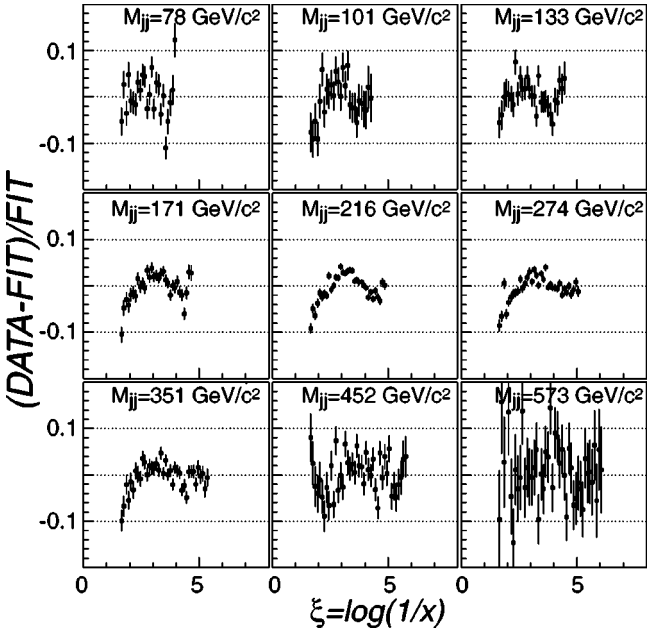

FIG. 15. The $(dN/d\xi_{Data} - dN/d\xi_{FIT})/dN/d\xi_{FIT}$ distribution for all dijet mass bins and for the restricted cone size $\theta_c = 0.47$ rad. Errors are statistical only. Fit curves correspond to Fig. 12 and are obtained by independently fitting each of the nine momentum distributions for the parameters K and Q_{eff}.

of the distribution, changing Q_{eff} will affect K. Table IV shows the values of K obtained from the fits of the momentum distributions with Q_{eff} fixed at 230 MeV for all 27 combinations.

To study K as a function of ϵ_g, one needs to evaluate ϵ_g for the data in each of the dijet mass bins. We did this by using the HERWIG 5.6 Monte Carlo program with CTEQ4M parton distribution functions. To evaluate the uncertainties, we used the CTEQ4HJ set. The predicted fraction of gluon jets monotonically decreases from $\epsilon_g \simeq 62$–$64\,\%$ of all jets at $M_{JJ} = 80$ GeV/c^2 to $\simeq 22$–26% at 600 GeV/c^2 (variations result from using different parton distribution functions).

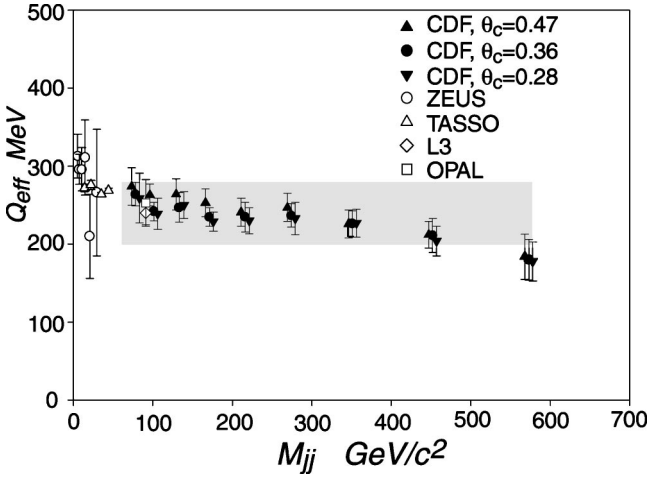

FIG. 16. Fitted values of the MLLA parameter Q_{eff} as a function of the dijet mass, for three cone sizes, $\theta_c = 0.28$, 0.36 and 0.47 rad. Each of the 27 distributions was fitted independently. The errors are dominated by the systematic uncertainties. Points corresponding to the cone sizes $\theta_c = 0.28$ and 0.47 are shifted left and right with respect to the dijet mass values they correspond to in order to avoid visual confusion. The reported value is $Q_{eff} = 230 \pm 40$ MeV, and the shaded area shows this range. For illustration, the data from *ee* and *ep* experiments are also shown. The slight drift in Q_{eff} may be due to higher order and/or non-perturbative effects.

Figure 17 shows K as a function of ϵ_g for the nine dijet mass data samples for the restricted cones of sizes $\theta_c = 0.28$, 0.36, and 0.47 rad. The results of the linear fits are shown on the plot. The error in r and the first error in $K_{LPHD}^{charged}$ are statistical and experimental systematic errors added in quadrature. A large fraction of the systematic error comes from varying the assumptions on the degree of correlation between individual experimental systematic uncertainties in the determination of K. We also fitted the same data using K's obtained from fits of the momentum distributions with Q_{eff} fixed at 190 and 270 MeV. The corresponding variations were included in the systematic error. The uncertainty resulting from the use of different parton distribution function (PDF) sets was small. The second error in K_{LPHD} reflects the theoretical uncertainty of ± 0.2 in $F_{nMLLA} = 1.3$. For the final reported values, we use the same approach as for Q_{eff}. Taking the unweighted average of the results for the three cone sizes, and treating the differences between the individual measured values and the average as an additional systematic uncertainty, we arrive at $r = N_{partons}^{g\text{-}jet}/N_{partons}^{q\text{-}jet} = 1.9 \pm 0.5$ and $K_{LPHD}^{charged} = 0.56 \pm 0.05 \pm 0.09$.

Table IV shows that, for each dijet mass value, K is stable with respect to the opening angle, as predicted by MLLA. However, we observe a slight decrease towards the smaller cone sizes. Given the strong correlation between the systematic uncertainties for the three cones, this small variation of K is statistically significant.

XII. PEAK POSITION OF THE MOMENTUM DISTRIBUTION

The value of Q_{eff} can also be extracted from the momentum distribution peak position, $\xi_0 = \log 1/x_0$ [see Eq. (4)]. This measurement is somewhat different from the direct fits to the MLLA-predicted function: this measured Q_{eff} depends only on the momentum distribution peak position, and does not depend on the distribution shape as a whole. Table V lists peak positions and corresponding values of Q_{eff} for the nine dijet mass bins and the three restricted cone sizes. Peak positions were found with a simple Gaussian fit in the vicinity of the distribution maximum ($\Delta\xi \simeq \pm 1$). The quality of the fit to the distributions for the peak position was good.

Figure 18 shows the correlation between the values of Q_{eff} extracted from the fits of shapes of the momentum distribution (Table II) and from the fit for the peak position (Table V). One can see that these two are in good agreement, a demonstration of self-consistency of the model.

To verify the predicted $E_{jet}\sin\theta_c/Q_{eff}$ scaling, we plotted the peak positions as a function of $M_{jj}\sin\theta_c = 2E_{jet}\sin\theta_c$ (Fig. 19). One can see that all points from three different opening angle data sets, being plotted versus $E_{jet}\sin\theta_c$, do

TABLE IV. Fitted values of K from inclusive momentum distributions of charged particles in cones of sizes 0.28, 0.36, and 0.47 rad around the jet axis for all available dijet mass samples with fixed parameter $Q_{eff}=230$ MeV. The first error is statistical and the second one is systematic. Note that the systematic uncertainties are strongly correlated.

Mean dijet mass (GeV/c^2)	Cone $\theta_c=0.28$	Cone $\theta_c=0.36$	Cone $\theta_c=0.47$
78	$K=0.558\pm0.003\pm0.053$	$K=0.591\pm0.003\pm0.047$	$K=0.598\pm0.003\pm0.048$
101	$K=0.567\pm0.004\pm0.038$	$K=0.593\pm0.004\pm0.044$	$K=0.605\pm0.004\pm0.040$
133	$K=0.545\pm0.003\pm0.039$	$K=0.563\pm0.003\pm0.046$	$K=0.570\pm0.003\pm0.042$
171	$K=0.552\pm0.001\pm0.039$	$K=0.565\pm0.001\pm0.040$	$K=0.580\pm0.001\pm0.050$
216	$K=0.535\pm0.001\pm0.040$	$K=0.547\pm0.001\pm0.042$	$K=0.562\pm0.001\pm0.043$
274	$K=0.525\pm0.001\pm0.049$	$K=0.541\pm0.001\pm0.044$	$K=0.549\pm0.001\pm0.045$
351	$K=0.504\pm0.001\pm0.047$	$K=0.519\pm0.001\pm0.046$	$K=0.525\pm0.001\pm0.047$
452	$K=0.469\pm0.002\pm0.046$	$K=0.482\pm0.002\pm0.045$	$K=0.489\pm0.002\pm0.049$
573	$K=0.424\pm0.004\pm0.051$	$K=0.435\pm0.004\pm0.051$	$K=0.442\pm0.004\pm0.050$

cluster along the same line, which confirms the $E_{jet}\sin\theta_c$ scaling. Assuming Q_{eff} is a constant, a fit to the CDF data in Table V gives $Q_{eff}=223\pm20$ MeV. This result has a smaller uncertainty than the one reported in Section XI, since we assume here that Q_{eff} is independent of E_{jet}. However, Fig. 16 suggests that this may not be true. We therefore prefer to quote the Q_{eff} value of Sec. XI as our final result.

Also plotted in the figure are the data points from ALEPH [30], DELPHI [31], L3 [20,32], Mark II [33], OPAL [21,34], TOPAZ [35] and ZEUS [29]. One should keep in mind that results quoted from other experiments were obtained by counting all particles in the full solid angle for e^+e^- experiments or the entire jet hemisphere for *ep* experiments, which technically corresponds to the opening angle $\theta_c=90°$. Therefore, these data did not verify the $E_{jet}\sin\theta_c$ scaling *per se*. However, the fact that all measurements from $p\bar{p}$, *ep* and *ee* collisions nicely overlap and complement each other has a significance of its own. First, it implies jet universality in various environments, and second, the validity of the MLLA description of jet fragmentation over two orders of magnitude in the range of jet energies.

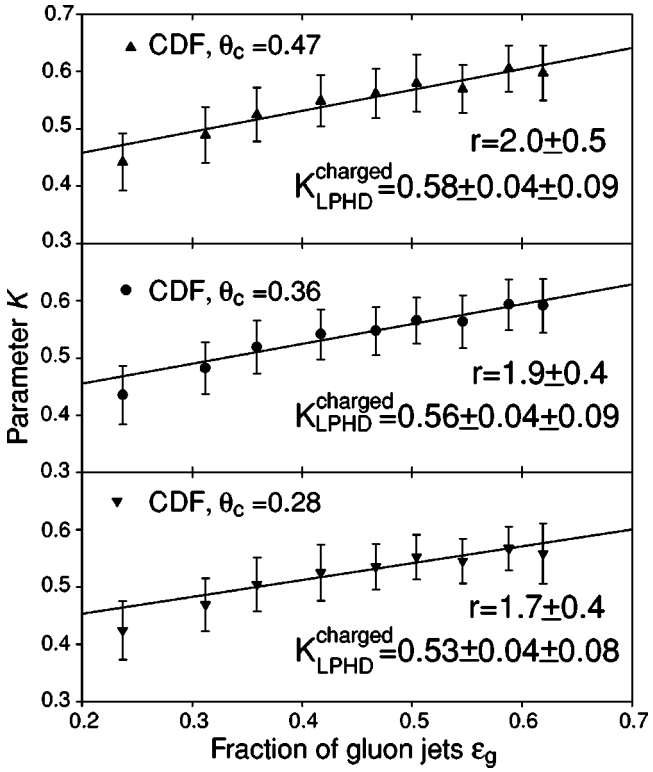

FIG. 17. Parameter K as a function of ϵ_g. The results of the linear fits for $r=N^{g\text{-}jet}_{partons}/N^{q\text{-}jet}_{partons}$ and $K^{charged}_{LPHD}$ [see Eq. (11)] are shown on the plot. The error in r and the first error in $K^{charged}_{LPHD}$ are combined statistical and systematic experimental uncertainties. The second error in $K^{charged}_{LPHD}$ corresponds to the assumed theoretical uncertainty of 0.2 on the value of 1.3 for F_{nMLLA}.

XIII. COMPARISONS TO HERWIG 5.6

In our previous studies [9], the HERWIG Monte Carlo program was found to overestimate the charged particle multiplicity in jets by approximately 11%. Here, we compared differential inclusive momentum distributions of charged particles to HERWIG 5.6 predictions and found the same trend.

Figure 20 shows the measured $dN/d\xi$ momentum distributions (central plots from Figs. 12–14) compared to predictions of HERWIG 5.6 that have been smeared for the detector response and corrected in the same manner as the data (i.e. no correction for the contamination from neighboring dijet mass bins was performed). HERWIG was scaled by a factor of 0.89 and, after rescaling, follows the data quite well. Other dijet mass bin data follow the same pattern.

Note that systematic uncertainties and corrections applied to the data are dominated by different effects in the soft and hard part of the spectrum (e.g. the CTC efficiency effects are more important for high momentum particles while the behavior of the soft side of the spectrum is more affected by the choice of the vertex cuts applied to remove γ conversions). This results in low correlations of the systematic uncertainties for the data in different ranges of ξ, making the 11% difference statistically significant.

Figure 1, which shows the dN/dk_T distributions in data and in HERWIG, is yet another confirmation of the same 11% effect. Note that this distribution has low correlation with the $dN/d\xi$ spectrum, as the tracks in a particular bin of the

TABLE V. Peak position ξ_0 and corresponding Q_{eff} for nine dijet mass bins and three opening angles. The first error is statistical and the second one is systematic.

Mean dijet mass (GeV/c^2)	Cone $\theta_c=0.28$	Cone $\theta_c=0.36$	Cone $\theta_c=0.47$
78	$\xi_0=2.64\pm0.01\pm0.05$	$\xi_0=2.78\pm0.01\pm0.05$	$\xi_0=2.91\pm0.01\pm0.05$
	$Q_{eff}=247\pm3\pm21$	$Q_{eff}=256\pm4\pm20$	$Q_{eff}=269\pm4\pm23$
101	$\xi_0=2.85\pm0.01\pm0.03$	$\xi_0=2.98\pm0.01\pm0.03$	$\xi_0=3.08\pm0.01\pm0.03$
	$Q_{eff}=233\pm4\pm11$	$Q_{eff}=238\pm5\pm12$	$Q_{eff}=262\pm5\pm14$
133	$\xi_0=3.00\pm0.01\pm0.04$	$\xi_0=3.15\pm0.01\pm0.04$	$\xi_0=3.26\pm0.01\pm0.05$
	$Q_{eff}=240\pm4\pm15$	$Q_{eff}=243\pm4\pm15$	$Q_{eff}=261\pm4\pm19$
171	$\xi_0=3.18\pm0.00\pm0.03$	$\xi_0=3.32\pm0.01\pm0.04$	$\xi_0=3.44\pm0.00\pm0.04$
	$Q_{eff}=231\pm1\pm12$	$Q_{eff}=235\pm2\pm14$	$Q_{eff}=251\pm2\pm17$
216	$\xi_0=3.33\pm0.00\pm0.04$	$\xi_0=3.47\pm0.00\pm0.04$	$\xi_0=3.61\pm0.00\pm0.04$
	$Q_{eff}=230\pm1\pm17$	$Q_{eff}=233\pm1\pm16$	$Q_{eff}=241\pm1\pm16$
274	$\xi_0=3.46\pm0.00\pm0.05$	$\xi_0=3.61\pm0.00\pm0.04$	$\xi_0=3.74\pm0.00\pm0.04$
	$Q_{eff}=238\pm1\pm19$	$Q_{eff}=236\pm1\pm15$	$Q_{eff}=246\pm1\pm18$
351	$\xi_0=3.63\pm0.01\pm0.04$	$\xi_0=3.80\pm0.01\pm0.04$	$\xi_0=3.96\pm0.01\pm0.05$
	$Q_{eff}=230\pm2\pm16$	$Q_{eff}=224\pm2\pm16$	$Q_{eff}=222\pm3\pm18$
452	$\xi_0=3.85\pm0.01\pm0.06$	$\xi_0=3.97\pm0.01\pm0.07$	$\xi_0=4.14\pm0.02\pm0.07$
	$Q_{eff}=207\pm4\pm21$	$Q_{eff}=216\pm4\pm25$	$Q_{eff}=212\pm7\pm25$
573	$\xi_0=4.06\pm0.03\pm0.07$	$\xi_0=4.21\pm0.03\pm0.10$	$\xi_0=4.35\pm0.02\pm0.09$
	$Q_{eff}=187\pm9\pm23$	$Q_{eff}=187\pm8\pm29$	$Q_{eff}=190\pm8\pm28$

dN/dk_T distribution come from many bins in the $dN/d\xi$ spectrum.

XIV. SUMMARY

We have measured inclusive momentum distributions of charged particles in jets for dijet events with a wide range of dijet masses, 80–600 GeV/c^2. The analysis was done for particles in restricted cones around the jet direction ($\theta_c=0.28$, 0.36, 0.47 rad).

The data were compared to calculations carried out in the framework of the modified leading log approximation in conjunction with the hypothesis of local parton-hadron duality. The data were found to follow the theoretical prediction

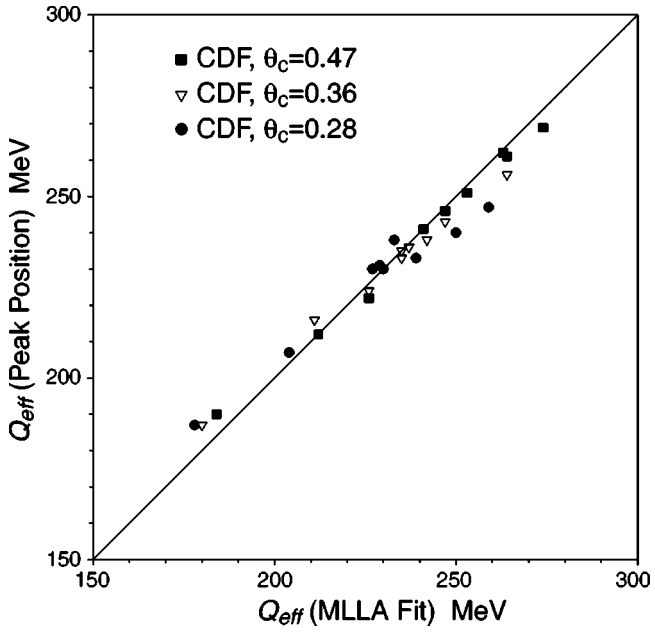

FIG. 18. Correlation between values of Q_{eff} from the fit according to Eq. (10) and from the Gaussian fit for peak position, Eq. (4). Uncertainties (not shown) are dominated by the systematic errors.

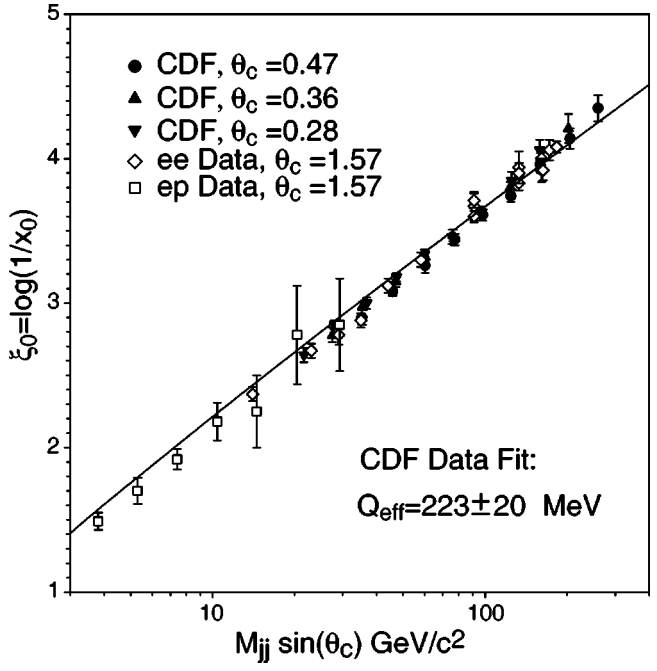

FIG. 19. Momentum distribution peak position as a function of $M_{jj}\sin\theta_c=2E_{jet}\sin\theta_c$. Also plotted in the figure are the data points from *ee* and *ep* experiments. A fit of the CDF data to Eq. (4) gives $Q_{eff}=223\pm20$ MeV.

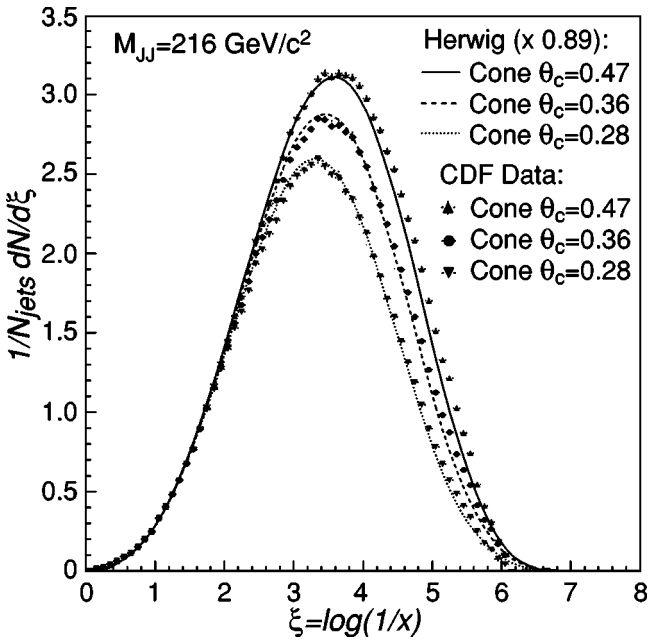

FIG. 20. Comparison of the inclusive momentum distribution of particles in jets in the restricted cones of size $\theta_c = 0.28$, 0.36 and 0.47 rad to HERWIG 5.6 predictions (scaled by 0.89), for dijet mass bin $M_{jj} = 216$ GeV/c^2.

rather well in the region where the MLLA is applicable. Quantitatively, we observe a 5–10 % discrepancy (see Fig. 15) between the experimental and theoretical shapes of the momentum spectra (note that the shape depends only on Q_{eff} and is independent of the choice of fit values for K, F_{nMLLA}, and r). A fit of the shape of the distributions yields $Q_{eff} = 230 \pm 40$ MeV with Q_{eff} decreasing for larger dijet masses. Measurement of the momentum distribution peak position agrees well with the MLLA. A fit of the evolution of the peak position with dijet mass gives $Q_{eff} = 223 \pm 20$ MeV, in agreement with the fits to the overall individual momentum distribution shapes. The $E_{jet}\sin\theta_c$ scaling is verified for the first time.

The fact that the content of quark and gluon jets in data varies with dijet mass allowed us to extract two MLLA parameters from the evolution of the charged particle momentum spectra: the ratio of multiplicities in gluon and quark jets, $r = N^{g\text{-}jet}_{partons}/N^{q\text{-}jet}_{partons} = 1.9 \pm 0.5$, and the ratio of the number of charged hadrons to the number of partons generated in a jet, $K^{charged}_{LPHD} = 0.56 \pm 0.10$.

HERWIG 5.6 was found to overestimate the overall multiplicity of charged particles in jets by about 11%. This excess appears to be approximately independent of particle momenta within a jet.

ACKNOWLEDGMENTS

The authors are very grateful to Yu. Dokshitzer, I. Dremin, V. Khoze, A. H. Mueller, V. Nechitailo, W. Ochs, R. Peschanski, and B. Webber for a number of very fruitful discussions. We thank the Fermilab staff and the technical staffs of the participating institutions for their vital contributions. This work was supported by the U.S. Department of Energy and the National Science Foundation; Italian Istituto Nazionale di Fisica Nucleare; Ministry of Science, Culture and Education of Japan; Natural Sciences and Engineering Research Council of Canada; the National Science Council of the Republic of China; Swiss National Science Foundation; the A.P. Sloan Foundation; the Bundeministerium fuer Bilding und Forschung, Germany; the Korea Science and Research Foundation (KoSEF); the Korea Research Foundation; and the Comision de Ciencia y Technologia, Spain.

[1] Yu. Dokshitzer and S. Troyan, XIX Winter School of LNPI, 1984, Vol. 1, p. 144.
[2] A.H. Mueller, Nucl. Phys. **B213**, 85 (1983); **B241**, 141(E) (1984).
[3] Yu.L. Dokshitzer, V.S. Fadin, and V.A. Khoze, Phys. Lett. **115B**, 242 (1982); A. Bassetto, M. Ciafaloni, G. Marchesini, and A.H. Mueller, Nucl. Phys. **B207**, (1982).
[4] Yu.L. Dokshitzer, V.A. Khoze, and S.I. Troyan, Int. J. Mod. Phys. A **7**, 1875 (1992); Z. Phys. C **55**, 107 (1992).
[5] E.D. Malaza and B.R. Webber, Phys. Lett. **149B**, 501 (1984).
[6] Yu.L. Dokshitzer, A.H. Mueller, V.A. Khoze, and S. Troyan, *Basics of Perturbative QCD* (Editions Frontieres, Paris, 1991).
[7] Ya.I. Azimov, Yu. Dokshitzer, V. Khoze, and S. Troyan, Z. Phys. C **27**, 65 (1985); **31**, 213 (1986).
[8] B.I. Ermolaev and V.S. Fadin, JETP Lett. **33**, 269 (1981); A.H. Mueller, Phys. Lett. **104B**, 161 (1981).
[9] CDF Collaboration, T. Affolder *et al.*, Phys. Rev. Lett. **87**, 211804 (2001).
[10] Yu. Dokshitzer (private communication).
[11] C.P. Fong and B.R. Webber, Phys. Lett. B **229**, 289 (1989); Nucl. Phys. **B335**, 54 (1991).
[12] S. Lupia and W. Ochs, Phys. Lett. B **418**, 214 (1998).
[13] I.M. Dremin and J.W. Gary, Phys. Lett. B **459**, 341 (1999).
[14] S. Catani, Yu. Dokshitzer, F. Fiorani, and B.R. Webber, Nucl. Phys. **B377**, 445 (1992).
[15] D. Amati and G. Veneziano, Phys. Lett. **83B**, 87 (1979); A. Bassetto, M. Ciafaloni, and G. Marchesini, *ibid.* **83B**, 207 (1979); G. Marchesini, L. Trentadue, and G. Veneziano, Nucl. Phys. **B181**, 335 (1981).
[16] JADE Collaboration, W. Bartel *et al.*, Z. Phys. C **9**, 315 (1981); CELLO Collaboration, H.J. Behrend *et al.*, Phys. Lett. **113B**, 427 (1982); TASSO Collaboration, M. Althoff *et al.*, Z. Phys. C **22**, 307 (1984); HRS Collaboration, D. Bender *et al.*, Phys. Rev. D **31**, 1 (1985).
[17] UA1 Collaboration, G. Arnison *et al.*, Nucl. Phys. **B276**, 253 (1986).
[18] CDF Collaboration, F. Abe *et al.*, Phys. Rev. Lett. **65**, 968 (1990).
[19] TASSO Collaboration, W. Braunschweig *et al.*, Z. Phys. C **47**, 187 (1990).
[20] L3 Collaboration, B. Adeva *et al.*, Phys. Lett. B **259**, 199 (1991).

[21] OPAL Collaboration, M.Z. Akrawy *et al.*, Phys. Lett. B **247**, 617 (1990).

[22] JADE Collaboration, W. Bartel *et al.*, Phys. Lett. **123B**, 460 (1983); HRS Collaboration, M. Derrick *et al.*, *ibid.* **165B**, 449 (1985); Mark II Collaboration, A. Petersen *et al.*, Phys. Rev. Lett. **55**, 1954 (1985); TASSO Collaboration, W. Braunschweig *et al.*, Z. Phys. C **45**, 1 (1989); AMY Collaboration, Y.K. Kim *et al.*, Phys. Rev. Lett. **63**, 1772 (1989).

[23] OPAL Collaboration, G. Alexander *et al.*, Phys. Lett. B **265**, 462 (1991); OPAL Collaboration, P.D. Acton *et al.*, Z. Phys. C **58**, 387 (1993); OPAL Collaboration, R. Akers *et al.*, *ibid.* **68**, 179 (1995); ALEPH Collaboration, D. Busculic *et al.*, Phys. Lett. B **346**, 389 (1995); OPAL Collaboration, G. Alexander *et al.*, *ibid.* **388**, 659 (1996); ALEPH Collaboration, D. Busculic *et al.*, *ibid.* **384**, 353 (1996); DELPHI Collaboration, P. Abreu *et al.*, Z. Phys. C **70**, 179 (1996); OPAL Collaboration, K. Ackerstaff *et al.*, Eur. Phys. J. C **1**, 479 (1998); DELPHI Collaboration, P. Abreu *et al.*, Phys. Lett. B **449**, 383 (1999); OPAL Collaboration, G. Abbiendi *et al.*, Eur. Phys. J. C **11**, 217 (1999); SLD Collaboration, Y. Iwasaki, SLAC-PUB-6597, 1994, presented at DPF 94, Albuquerque, NM, 1994; SLD Collaboration, Y. Iwasaki, SLAC preprint, SLAC-R-95-460, Stanford, 1995.

[24] F. Abe *et al.*, Nucl. Instrum. Methods Phys. Res. A **271**, 387 (1988); D. Amidei *et al.*, *ibid.* **350**, 73 (1994); P. Azzi *et al.*, *ibid.* **360**, 137 (1995).

[25] F. Abe *et al.*, Phys. Rev. D **45**, 1448 (1992).

[26] G. Marchesini, B.R. Webber, G. Abbiendi, I.G. Knowles, M.H. Seymour, and L. Stanco, Comput. Phys. Commun. **67**, 465 (1992).

[27] H.L. Lai, J. Huston, S. Kuhlmann, F. Olness, J. Owens, D. Soper, W.K. Tung, and H. Weerts, Phys. Rev. D **55**, 1280 (1997).

[28] J. Huston, E. Kovacs, S. Kuhlmann, H.L. Lai, J.F. Owens, D. Soper, and W.K. Tung, Phys. Rev. Lett. **77**, 444 (1996).

[29] ZEUS Collaboration, M. Derrick *et al.*, Z. Phys. C **67**, 93 (1995).

[30] ALEPH Collaboration, D. Buskulic *et al.*, Z. Phys. C **73**, 409 (1997).

[31] DELPHI Collaboration, P. Abreu *et al.*, Phys. Lett. B **275**, 231 (1992); Z. Phys. C **73**, 229 (1997).

[32] L3 Collaboration, M. Acciarri *et al.*, Phys. Lett. B **444**, 569 (1998).

[33] MARK II Collaboration, A. Petersen *et al.*, Phys. Rev. D **37**, 1 (1988).

[34] OPAL Collaboration, G. Abiendy *et al.*, Z. Phys. C **72**, 191 (1996); **75**, 193 (1997).

[35] TOPAZ Collaboration, R. Itoh *et al.*, Phys. Lett. B **345**, 335 (1995).